












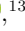






## Cold Gas and Star Formation in the Phoenix Cluster with JWST

MICHAEL REEFE <sup>1,\*</sup> MICHAEL McDONALD <sup>1</sup> MARIOS CHATZIKOS <sup>2</sup> JEROME SEEBECK,<sup>3</sup> RICHARD MUSHOTZKY <sup>3</sup>,  
SYLVAIN VEILLEUX <sup>3</sup>, STEVEN W. ALLEN <sup>4,5,6</sup> MATTHEW BAYLISS <sup>7</sup> MICHAEL CALZADILLA <sup>1</sup>,  
REBECCA CANNING <sup>8</sup> MEGAN DONAHUE <sup>9</sup> BENJAMIN FLOYD <sup>8,10</sup> MASSIMO GASPARI <sup>11</sup>,  
JULIE HLAVACEK-LARRONDO <sup>12</sup> BRIAN MCNAMARA <sup>13</sup> HELEN RUSSELL <sup>14</sup> ARNAB SARKAR <sup>1</sup> KEREN SHARON <sup>15</sup>,  
AND TAWEEWAT SOMBOONPANYAKUL <sup>16</sup>

<sup>1</sup>*Kavli Institute for Astrophysics & Space Research, Massachusetts Institute of Technology, Cambridge, MA 02139, USA*

<sup>2</sup>*Department of Physics & Astronomy, University of Kentucky, Lexington, KY 40506, USA*

<sup>3</sup>*Department of Astronomy & Joint Space-Science Institute, University of Maryland, College Park, College Park, MD 20740, USA*

<sup>4</sup>*Kavli Institute for Particle Astrophysics and Cosmology, Stanford University, 452 Lomita Mall, Stanford, CA 94305, USA*

<sup>5</sup>*Department of Physics, Stanford University, 382 Via Pueblo Mall, Stanford, CA 94305, USA*

<sup>6</sup>*SLAC National Accelerator Laboratory, 2575 Sand Hill Road, Menlo Park, CA 94025, USA*

<sup>7</sup>*Department of Physics, University of Cincinnati, Cincinnati, OH 45221, USA*

<sup>8</sup>*Institute of Cosmology & Gravitation, University of Portsmouth, Dennis Sciama Building, Portsmouth, PO1 3FX, UK*

<sup>9</sup>*Department of Physics and Astronomy, Michigan State University, East Lansing, MI 48824, USA*

<sup>10</sup>*Department of Physics and Astronomy, University of Missouri-Kansas City, Flarsheim Hall, 5110 Rockhill Road, Kansas City, MO 64110, USA*

<sup>11</sup>*Department of Physics, Informatics and Mathematics, University of Modena and Reggio Emilia, 41125 Modena, Italy*

<sup>12</sup>*Department of Physics, Université de Montréal, Montreal, QC H3T 1J4, Canada*

<sup>13</sup>*Department of Physics and Astronomy, University of Waterloo, Waterloo, ON N2L 3G1, Canada*

<sup>14</sup>*School of Physics & Astronomy, University of Nottingham, University Park, Nottingham NG7 2RD, UK*

<sup>15</sup>*Department of Astronomy, University of Michigan, 1085 S. University Ave, Ann Arbor, MI 48109, USA*

<sup>16</sup>*Department of Physics, Faculty of Science, Chulalongkorn University, 254 Phayathai Road, Pathumwan, Bangkok 10330, Thailand*

### ABSTRACT

We present integral field unit observations of the Phoenix Cluster with the *JWST* Mid-infrared Instrument’s Medium Resolution Spectrometer (MIRI/MRS). We focus this study on the molecular gas, dust, and star formation in the brightest cluster galaxy (BCG). We use precise spectral modeling to produce maps of the silicate dust, molecular gas, and polycyclic aromatic hydrocarbons (PAHs) in the inner  $\sim 50$  kpc of the cluster. We have developed a novel method for measuring the optical depth from silicates by comparing the observed  $\text{H}_2$  line ratios to those predicted by excitation models. We provide updated measurements of the total molecular gas mass of  $2.2^{+0.4}_{-0.1} \times 10^{10} M_\odot$ , which agrees with CO-based estimates, providing an estimate of the CO-to- $\text{H}_2$  conversion factor of  $\alpha_{\text{CO}} = 0.9 \pm 0.2 M_\odot \text{pc}^{-2} (\text{K km s}^{-1})^{-1}$ ; an updated stellar mass of  $M_* = 2.6 \pm 0.5 \times 10^{10} M_\odot$ ; and star formation rates averaged over 10 and 100 Myr of  $\langle \text{SFR} \rangle_{10} = 1340 \pm 100 M_\odot \text{yr}^{-1}$  and  $\langle \text{SFR} \rangle_{100} = 740 \pm 80 M_\odot \text{yr}^{-1}$ , respectively. The  $\text{H}_2$  emission seems to be powered predominantly by star formation within the central  $\sim 20$  kpc, with no need for an extra particle heating component as is seen in other BCGs. Additionally, we find nearly an order of magnitude drop in the star formation rates estimated by PAH fluxes in cool core BCGs compared to field galaxies, suggesting that hot particles from the intracluster medium are destroying PAH grains even in the centralmost 10s of kpc.

*Keywords:* Galaxy clusters (584) — Infrared astronomy(786) — Cooling flows (2028) — Active galaxies (17) — Elliptical galaxies (456) — Starburst galaxies (1570)

## 1. INTRODUCTION

The hot intracluster medium (ICM) that permeates clusters of galaxies exists at temperatures of order  $10^7$  K and emits thermal bremsstrahlung radiation in the X-ray. This radiation causes it to lose energy and cool down over time. Once the gas cools to  $\sim 10^{6.5}$  K, it may start to radiate through other mechanisms, primarily metal line emission, increasing the rate of cooling. The many complex physical processes that contribute to the cooling rate of gas are commonly conglomerated into a single entity called the *cooling function*  $\Lambda(T)$  (i.e. Sutherland & Dopita 1993). This, in combination with the initial thermal energy (per unit volume) of the gas  $\mathcal{E}$ , can give an idea of the overall *cooling time*,  $t_{\text{cool}} \sim \mathcal{E}/n^2\Lambda \propto T^{1/2}n^{-1}$ . If the initial temperature of the gas is not too high, and its density is not too low, then a *cooling flow* may develop within cooling times less than the age of the universe, meaning they should be observable (Fabian et al. 1984). In the classical (isobaric) picture, a cooling flow unfolds as follows (see, e.g., Mo et al. 2010). Consider a parcel of ICM gas that cools by an incremental amount—its temperature drops, and by the ideal gas law so does its pressure. The weight of the surrounding gas now pushes on the parcel, causing it to move inwards and increase in density. The change in density causes a corresponding change in pressure until it can again reach a state of equilibrium with the surrounding gas.

Studying the cold gas content and stellar populations in galaxy clusters is crucial for understanding the end stages of these cooling flows, which illuminates how they affect the evolution of brightest cluster galaxies (BCGs). Ideal cooling flows like described above cannot exist in nature because cooling can never be 100% efficient. Heating, turbulence, and magnetic fields are just a few examples of physical processes that reduce cooling efficiency and prevent unabated cooling flows from developing. Indeed, if the gas were somehow able to cool unabated from the hot  $\sim 10^7$  K atmosphere to the cold 10 K molecular phase and rapidly form stars, we should observe star formation rates (SFRs) in BCGs of a similar magnitude to the classical cooling rates measured from the ICM. However, in reality the observed SFRs are typically suppressed by 2 orders of magnitude relative to the cooling rates (McNamara & O’Connell 1989; Allen 1995; Crawford et al. 1999; Hicks & Mushotzky 2005; Edwards et al. 2007; Hatch et al. 2007; O’Dea et al. 2008; McDonald et al. 2010, 2018; Hoffer et al. 2012; Rawle et al. 2012; Donahue et al. 2015; Mittal et al. 2015; Molendi et al. 2016; Calzadilla et al. 2023). Additionally, cooling flows are expected to last for a sig-

nificant fraction of a cluster’s lifetime based on the incidence rate of cool core clusters in the general galaxy cluster population. For timescales of Gyr, the amount of molecular gas formed should be on the order  $10^{11}$ – $10^{12} M_{\odot}$ . Nevertheless, observed molecular gas masses consistently fall short of this prediction, typically ranging from  $10^8$ – $10^{10} M_{\odot}$  (Edge 2001; Salomé & Combes 2003; Salomé et al. 2008). This, in conjunction with the low SFRs, is evidence that a large fraction of the gas is not able to fully cool and is being reheated, likely by feedback from an active galactic nucleus (AGN) in the core (see reviews by McNamara & Nulsen 2007; Fabian 2012; Gaspari et al. 2020). Thus, the classical steady isobaric picture of cooling flows is most likely not an accurate representation of how cooling actually takes place in these clusters. Simulations and theories now suggest that cooling proceeds as a more chaotic, turbulent cascade of condensing cold clouds that periodically precipitate onto and fuel accretion (feeding) and feedback episodes of the central supermassive black hole (SMBH; Gaspari et al. 2011; Prasad et al. 2015; Li et al. 2017; Gaspari et al. 2018).

Dust content is also important to consider in the context of cooling flows—dust grains are closely linked with the cold molecular gas, acting as “seeds” for the gas to clump into star forming regions and filaments, boosting condensation and the cooling cascade and enriching the stellar populations. The presence of dust can inform the presence of cold gas and stars, and vice versa (Calura et al. 2008; Kaviraj et al. 2012). It is especially important when considering attenuation effects, which are dependent on both wavelength and geometry and can complicate measurements of the cooling rates and inferences made from these measurements. Cooling rates measured from emission lines in the UV, such as O VI  $\lambda\lambda 1032, 1038\text{\AA}$ , can be significantly underestimated if an extinction correction is not taken into account. Absorption effects may also partially explain why many lines in the soft X-ray regime below  $10^{6.5}$  K seem to be absent or much weaker than expected in many systems (Canizares et al. 1988; David et al. 2001; Peterson et al. 2003), implying much of the cooling gas is “hidden,” but may still be fueling massive cooling flows down to the molecular gas regime (Fabian et al. 2022, 2023).

The Phoenix Cluster (SPT-CLJ2344-4243; Williamson et al. 2011; McDonald et al. 2012) is an interesting case study in the field of cooling flows. Its extreme  $500$ – $800 M_{\odot} \text{ yr}^{-1}$  starburst represents  $\sim 10$ – $20\%$  of the  $3,800 M_{\odot} \text{ yr}^{-1}$  classical cooling rate (compared to the typical 1%; McDonald et al. 2012), and it contains a massive  $2.1 \pm 0.3 \times 10^{10} M_{\odot}$  reservoir of cold molecular gas (Russell et al. 2017), both signs which

point to it being one of the most rapid and uninhibited cooling flows in the known universe. This makes it an ideal playground to study the effects of large-scale cooling on host galaxies. However, due to the complex nature of this system, which hosts an extremely luminous type II QSO on top of a massive cooling flow, many of these measurements are marred by systematic uncertainties relating to how much of the underlying emission can be attributed to the QSO, how much dust extinction there is, and the metallicity of the ICM. The molecular gas mass estimate in particular relies on an uncertain conversion factor between CO and H<sub>2</sub>,  $\alpha_{\text{CO}}$ , which may vary by a factor of a few depending on the density, temperature, and metallicity of the molecular clouds (Bolatto et al. 2013).

Our recent work (Reefe et al. 2025, in press; hereafter R25) looked at this unique cluster through an infrared lens with observations using *JWST*'s Mid-infrared Instrument in Medium Resolution Spectroscopy mode (MIRI/MRS), which has the advantage of being in a wavelength regime with essentially no extinction. R25 focused on the intermediate-temperature ( $10^{5.5}$  K) coronal gas, using the high-ionization [Ne VI], [Ne V], [Fe VIII], [Fe VII], and [Mg VII] lines to reveal the morphology, kinematics, and cooling rate of the gas in between the hot and cold phases. In this work, we wish to examine this same dataset through a new lens, now with a focus on the molecular gas, dust, and star formation. The mid-infrared spectral range covered by MIRI/MRS is rich in spectral features from warm molecular gas (the rovibrational H<sub>2</sub> emission lines), dust (the thermal dust continuum and the 9.7  $\mu\text{m}$  silicate absorption feature), and very small dust grains known as Polycyclic Aromatic Hydrocarbons (PAHs, which exhibit broad emission features). We have 4 primary goals with this analysis, which we tackle in sequence throughout this paper: (1) Understand the morphology of the warm molecular gas, dust, and PAHs and how they relate to heating and feedback sources (i.e. radio jets) and the other gas phases, most notably the cold molecular gas seen in CO; (2) obtain an independent measurement of the total molecular gas mass directly from the H<sub>2</sub> emission lines, without relying on the uncertain  $\alpha_{\text{CO}}$  conversion factor; (3) use this new data to get better constraints on the star formation history, and a more precise measurement of the current star formation rate; and (4) use correlations and known scaling relations between IR spectral features to obtain constraints on the importance of different heating mechanisms in exciting the molecular gas and dust, and compare these with the typical cool core BCG population.

To aid with our fourth goal, we build upon the work of Donahue et al. (2011), hereafter D11, who studied a sample of cool core (CC) BCGs using infrared spectra and photometry from the *Spitzer Space Telescope*. Correlations between the emission features from dust, PAHs, molecular gas, and warm ionized gas are often seen in galaxies of different types and can give insights into the dominant physical mechanisms that power the emission. Gas and dust can be heated through star formation, cosmic rays, suprathermal ICM electrons, photoelectrons ejected from dust grains, shocks, and/or AGN feedback in the form of mechanical radio jets, radiative winds, and turbulence (Hlavacek-Larrondo et al. 2015; Gaspari et al. 2011; Prasad et al. 2015). D11 found a number of such correlations in the CC BCG population using spectral features in the mid-infrared, and the Infrared Spectrograph on *Spitzer* covers a very similar spectral range as MIRI/MRS, so we find these correlations useful as a comparison point for the Phoenix Cluster.

This paper is organized as follows. The observations and data reduction methods are presented in §2. Then, §3 goes over the analysis, subdivided by our individual goals as outlined above: §3.1 covers the gas and dust morphology and the gas mass, §3.2 covers the stellar populations and star formation, and §3.3 covers the correlation analysis. §4 discusses our findings in the context of the theory that Phoenix contains an undermassive SMBH, and goes over the expected evolution of the cluster in this scenario. We then summarize our findings in §5. Throughout this work, we assume a flat  $\Lambda$ CDM cosmology with  $\Omega_m = 0.27$ ,  $\Omega_\Lambda = 0.73$ , and  $H_0 = 70$  km s<sup>-1</sup> Mpc<sup>-1</sup>.

## 2. OBSERVATIONS

### 2.1. Data Collection

We obtained *JWST* MIRI/MRS observations of the Phoenix Cluster on UTC 2023 July 27–28 with program ID 2439. Exposures were taken in all channel/band combinations. The SHORT (A) band exposures were the longest, at 6.95 hours (since the primary science goal of this program was measuring the [Ne VI] emission, i.e. R25), while the MEDIUM (B) and LONG (C) band exposures were 51.0 and 85.8 minutes, respectively. Dedicated background exposures were also taken, with exposure times of 51.0, 16.8, and 25.2 minutes. On-source exposures used a 4-point dither pattern while background exposures used a 2-point dither pattern. In the rest-frame of Phoenix A ( $z = 0.597$ ), MIRI/MRS covers a wavelength range of 3.1–17.5  $\mu\text{m}$ .

### 2.2. Data Reduction

Here, we provide a brief overview of the general steps taken in the data reduction, cleaning, and correction processes. For full details on these procedures, see R25. We use the STScI pipeline version 1.12.3 and CRDS context `jwst.1140.pmap` to reduce the MIRI/MRS data. We use a few non-standard settings, including more aggressive cosmic ray flagging (lowering the jump rejection threshold to  $3.5\sigma$  and enabling cosmic ray shower flagging<sup>1</sup>), 2D residual fringe correction (removing fixed-frequency modulations in the spectrum caused by standing waves<sup>2</sup>), and 2D pixel-by-pixel background subtraction<sup>3</sup>. We also perform a few additional data cleaning procedures. We remove hot/warm pixels by flagging outliers in the background exposures and masking them in both the background and science frames, following Spilker et al. (2023). The thresholds for flagging outliers were chosen by hand for each channel and tried to keep a balance between keeping as much data as possible and making sure to exclude obviously bad pixels. The (low, high) threshold pixel values for channels 1 & 2, 3, and 4, after subtracting the median, were  $(-0.14, +0.13)$ ,  $(-0.16, +0.10)$ , and  $(-0.16, +0.27)$ , respectively. We also remove stripe artifacts caused by cosmic ray hits, also following Spilker et al. (2023). Additionally, we rescale the data to account for the loss in sensitivity over time of MIRI. We also replace the pipeline-produced errors with our own estimates of the pixel-by-pixel scatter by measuring the RMS variation between the data and a cubic spline fit with a spacing of 7 pixels between knots (masking emission lines).

Our data has a bright point source due to the IR-bright QSO at the center of Phoenix A. We are, therefore, interested in modeling the PSF of MIRI/MRS. To do so, we use data of the bright star 16 Cygni B from program ID 1538. We shift the centroid of the star to match the position of our Phoenix A data, normalize such that it integrates to 1 at each wavelength slice, and fit a cubic spline along the wavelength axis with 100 pixels between each knot. The normalization is done to remove the spectral shape of the star, and the spline fitting is done to reduce the noise in the extracted PSF profile, which should only vary gradually with wavelength. Again, for full details on these procedures, refer to R25. See Figure 1 for an example spectrum and model of a bright off-nuclear spaxel.

### 3. RESULTS & DISCUSSION

<sup>1</sup> JWST pipeline cosmic ray snowball/shower information

<sup>2</sup> JWST Pipeline fringing information

<sup>3</sup> JWST pipeline background subtraction information

#### 3.1. Gas & Dust Content

We use the Likelihood Optimization of gas Kinematics in IFUs (LOKI)<sup>4</sup> code to perform least-squares fits of the spectra in each spaxel. During the fitting procedure, the light from each spaxel is separated into a host galaxy component and a QSO component. The former traces the underlying emission from the gas, dust, and stars within and along the line of sight of the BCG at the location of the spaxel. The latter traces light from the central QSO that has been dispersed according to the PSF and contaminates the observed spectrum of the spaxel. For these fits, we follow the methods of R25.

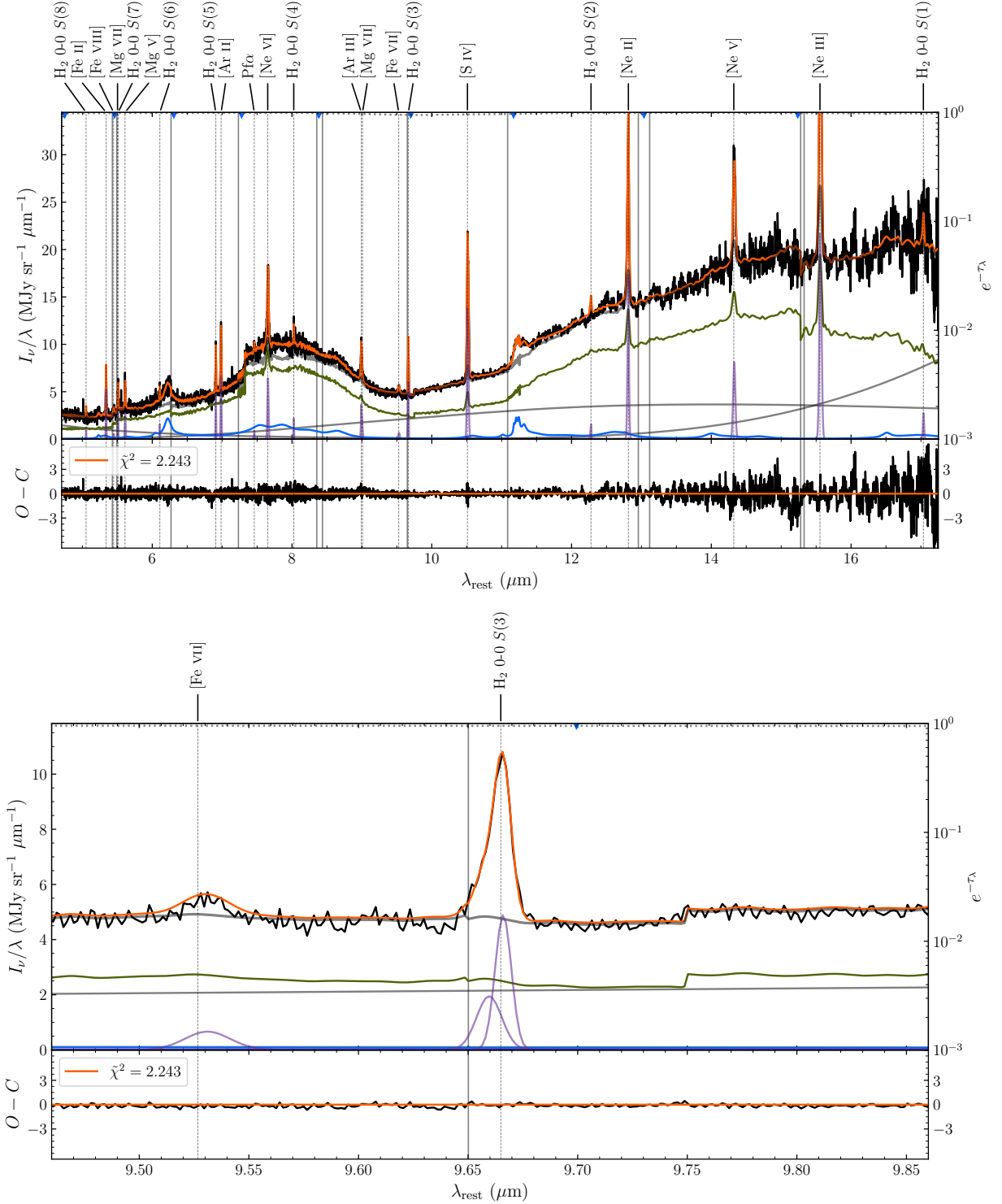
##### 3.1.1. Silicate Dust Obscuration

We first perform a set of initial fits for each individual channel. In these initial fits, the recovered optical depth  $\tau$  of the host galaxy is unreliable because the QSO spectrum outshines the host galaxy within  $\sim 15$  kpc of the center (due to the PSF). The faint continuum of the host galaxy becomes dominated by instrumental systematics that make it difficult to measure  $\tau$  from the shape of the silicate absorption feature. As such, we measure the optical depth of the host galaxy using an independent method that only relies on the flux ratios of the rotational  $H_2$  lines obtained from these initial fits. In contrast to the continuum and higher ionization lines, the  $H_2$  lines have a much smaller equivalent width in the QSO spectrum compared to the host galaxy, so their fluxes are dominated by their host galaxy fluxes away from the nucleus. Most of these lines are unaffected by extinction, but there is one—the  $H_2$  0-0  $S(3)$  line—that fortuitously lands very near the peak of the  $9.7 \mu\text{m}$  silicate absorption feature (see Figure 1). We therefore use the  $S(4)/S(3)$  line ratio as a proxy for the extinction. We estimate what this ratio should be in the absence of extinction by fitting excitation models with the  $S(3)$  line masked out (see §3.1.3). We then compare this to our observed  $S(4)/S(3)$  ratio to obtain an estimate of the optical depth at the peak of the silicate absorption feature:

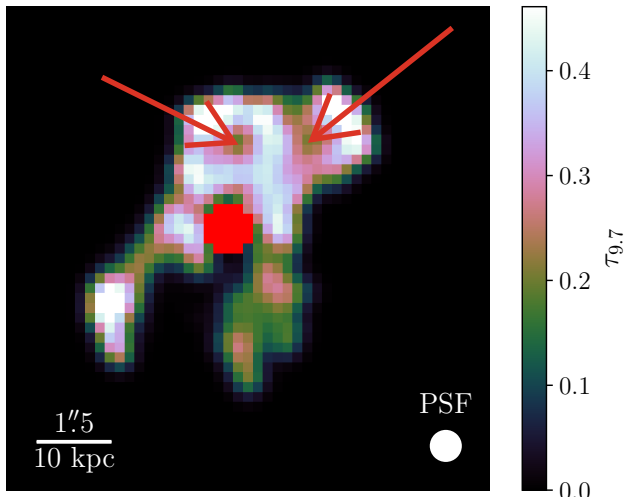
$$\tau_{9.7} \approx \ln \frac{[S(4)/S(3)]_{\text{obs}}}{[S(4)/S(3)]_{\text{int}}} \quad (1)$$

This results in the optical depth map shown in Figure 2. Note once again that this is the optical depth just in the host galaxy, and does not accurately represent the obscuration of the QSO at the center (marked by the red spaxels). The estimated uncertainty in these measurements is  $\simeq 5\%$  in the brightest spaxels, rising up to a

<sup>4</sup> <https://github.com/Michael-Reefe/Loki.jl>



**Figure 1.** The MIRI/MRS spectrum of a bright off-nuclear spaxel. In each plot, the upper panel shows the data, model, and individual model components, and the lower panel shows the residuals. The data is presented in black, the full model in orange, thermal dust continua in gray, PAH emission in blue, emission lines in purple, and the QSO PSF model in green. The extinction profile is shown by the gray dotted line across the top of the plots and is read from the right axis. Emission lines are labeled with vertical dashed lines, and boundaries between MIRI/MRS channels are labeled with blue triangles at the top of the plots. The top plot shows the full spectrum, incorporating data from channels 2–4. The bottom plot shows a zoom-in of the same spectrum around the H<sub>2</sub> 0-0 S(3) emission line. The vertical jumps that occur in the QSO PSF component are due to differences in the size and shape of the PSF between MIRI/MRS channels.



**Figure 2.** The optical depth of the Phoenix cluster at  $9.7 \mu\text{m}$  from the silicate absorption feature, estimated using the  $\text{H}_2$  line ratios. Note that the central spaxels are masked out (denoted by red) since the  $\text{H}_2$  lines are not significantly detected in these spaxels.

median of  $\simeq 20\%$  in all spaxels, due to a combination of uncertainties in the measured and modeled line ratios.

The optical depth at  $9.7 \mu\text{m}$  is a direct tracer of the column density of silicate dust grains, which create broad absorption features in the MIR through bending and stretching modes. We can see that the silicates are concentrated north of the nuclear region where they form two loop structures (marked with red arrows), with two filaments extending to the south and southeast. The overall structure is reminiscent of the  $E(B-V)$  maps obtained from the UV continuum (McDonald et al. 2013) and Balmer lines (McDonald et al. 2014), showing that the silicate dust grains generally follow the rest of the dust, but the substructure in the silicates is distinct, particularly in the loops. The structure is statistically significant given our relatively low uncertainties in the brighter spaxels.

### 3.1.2. The Molecular Gas Phase

After obtaining the optical depth map from the excitation models, we run a second iteration of our individual channel fits while locking the optical depth of the host galaxy to these values, with the primary purpose of obtaining more accurate molecular  $\text{H}_2$  line fluxes. Note that this analysis inherently assumes that the extinction of the line-emitting  $\text{H}_2$  gas is the same as the extinction of the thermal continuum-emitting dust. Previous studies from Veilleux et al. (2009) have suggested that there may not be a simple 1:1 correlation between these two optical depths, with the emission lines and PAHs being systematically extinguished at lower optical depths than the

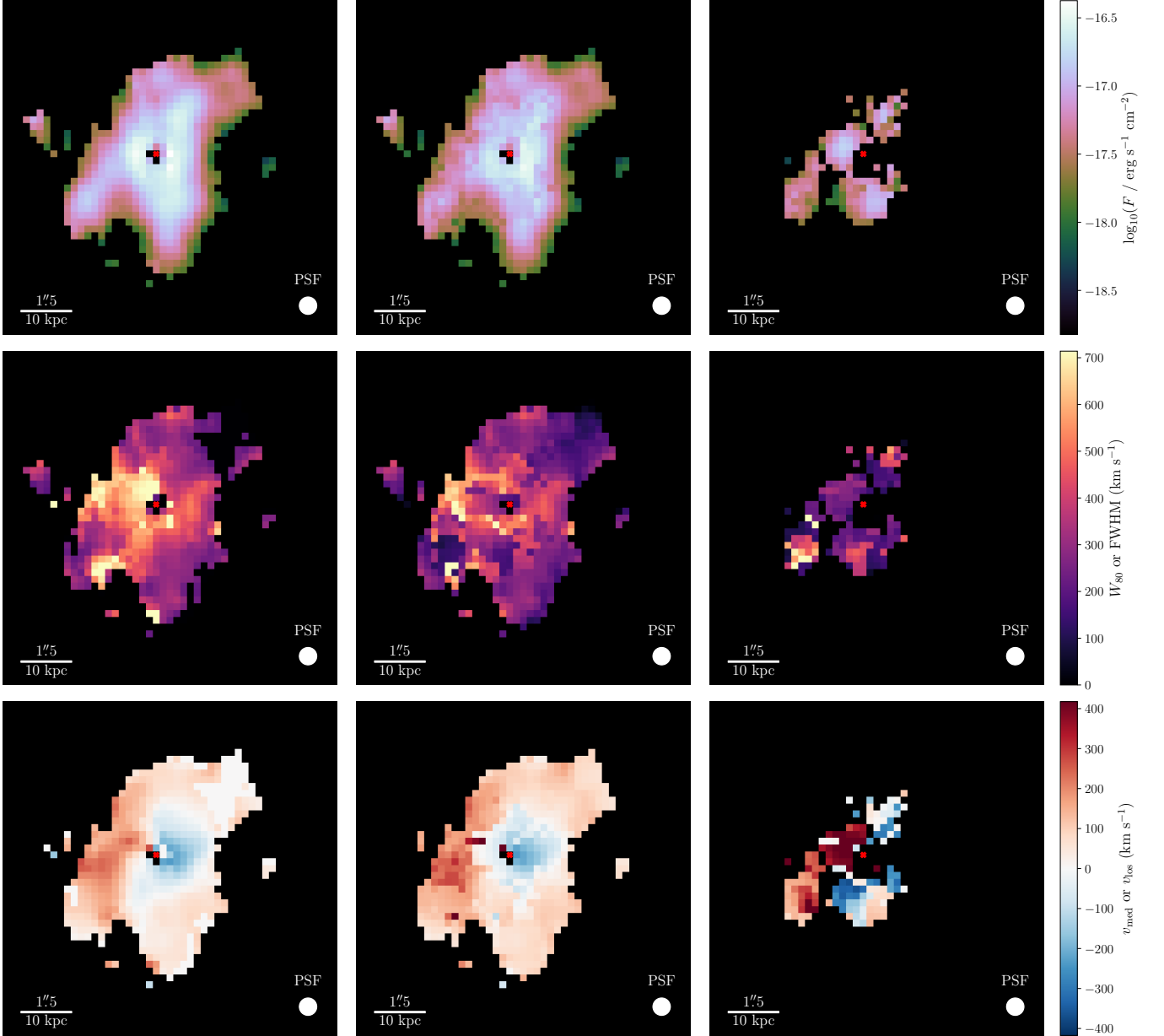
continuum. We find that due to the low continuum level of the host galaxy relative to the QSO, we require some external constraint on the optical depth parameter to keep it within a parameter space that makes physical sense, and this assumption does not significantly hinder our fitting results. Throughout the rest of our analysis, we are primarily concerned with using optical depths to correct the flux values of emission lines, so the values derived using the  $S(4)/S(3)$  line ratios are the most relevant and accurate ones to use.

The flux, velocity width, and velocity shift of the  $S(3)$  line are shown in Figure 3. The line is decomposed into 2 Gaussian velocity components with distinct centers and widths—the leftmost column shows the combined values of both components, the middle column shows the brighter component, and the rightmost column shows the dimmer component. The morphology of the  $\text{H}_2$  lines strongly resembles the CO emission from Russell et al. (2017), though it is slightly more extended and diffuse in comparison, owing to it tracing marginally warmer gas than the CO. The  $\text{H}_2$  and CO both share three filamentary structures extending to the southeast, south, and northwest, and a bright extended nuclear region. The brighter  $\text{H}_2$  component has broader line widths of up to  $600 \text{ km s}^{-1}$  and smaller velocity shifts within  $|v| \lesssim 200 \text{ km s}^{-1}$ . This component largely traces the motions of unresolved clouds drifting slowly in the large-scale macro turbulence of the BCG’s star-forming regions. The dimmer component is significantly more narrow, with line widths of  $\sim 200\text{--}300 \text{ km s}^{-1}$ , and with faster shifts up to  $\pm 400 \text{ km s}^{-1}$ . This component captures the bulk motion of the high-velocity gas clouds in the filaments that feed into or out of the nucleus, fueling episodes of chaotic cold accretion (see i.e. Gaspari et al. 2018). The other  $\text{H}_2$  lines generally follow the same morphology as the  $S(3)$  line, with varying levels of brightness. We see that, in general, the warm molecular gas traces regions of enhanced star formation revealed by observations in the optical and UV (McDonald et al. 2014, 2015) and wraps around the cavities in the X-ray emitting ICM (McDonald et al. 2015).

### 3.1.3. Molecular Gas Mass

Using the fluxes for the set of pure rotational  $\text{H}_2$  lines that fall within our wavelength range,  $S(2)$  to  $S(8)$  (excluding  $S(1)$  since it falls in channel 4C where the data quality is significantly deteriorated), we construct excitation diagrams of the upper level column densities of these transitions and fit a continuous temperature model from Togi & Smith (2016):

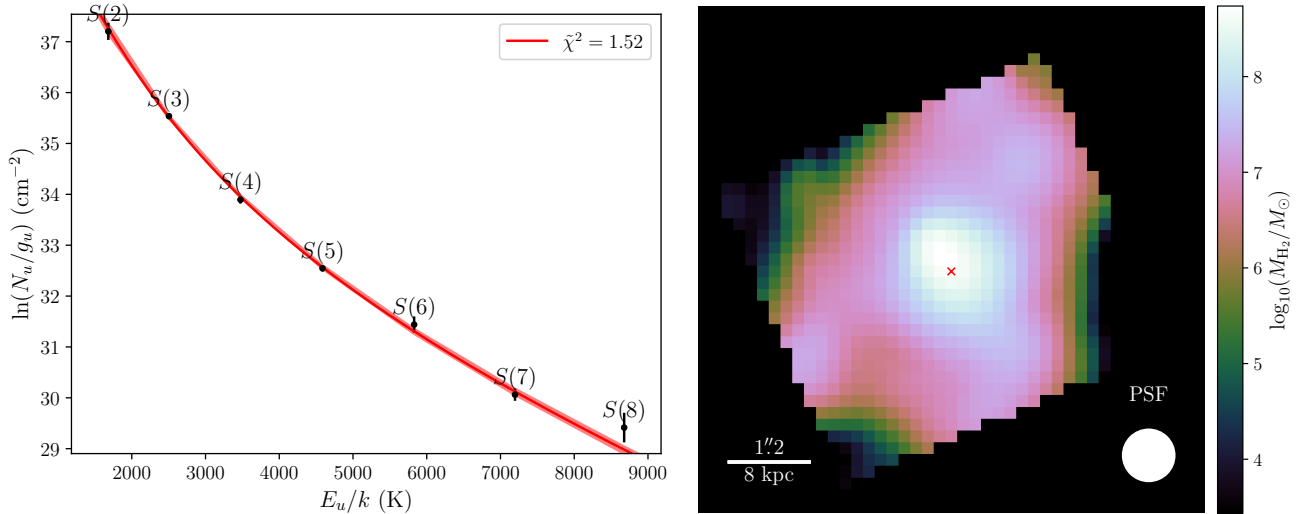
$$\frac{N_u}{g_u} = \frac{N_{\text{tot}}(n-1)}{T_\ell^{1-n} - T_u^{1-n}} \int_{T_\ell}^{T_u} \frac{e^{-E_u/kT}}{Z(T)} T^{-n} dT \quad (2)$$



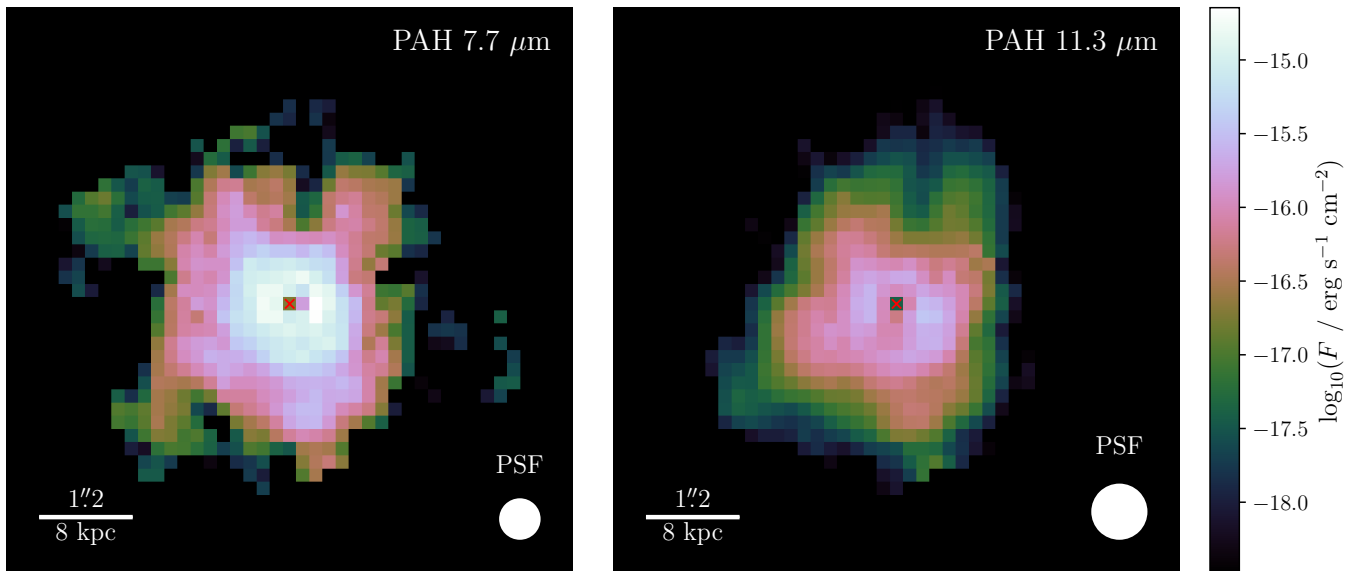
**Figure 3.** Maps of the  $\text{H}_2$  0-0  $S(3)$  line over the channel 3 FOV. The top row shows the flux with a logarithmic colormap. The left panel is the total flux, and the right 2 panels show the flux of the individual components. The middle row shows the line width in  $\text{km s}^{-1}$ . The left panel is  $W_{80}$ , the width containing 80% of the flux, and the right 2 panels are the FWHMs of the individual components. The bottom row shows the LOS velocity in  $\text{km s}^{-1}$ . The left panel is the median velocity, and the right 2 panels are the LOS velocities of the individual components. In all of the middle and right column, the components are sorted by flux, with the middle column having the larger flux and the right column having the smaller flux. Only spaxels with an  $S/N \geq 3$  are shown.

where  $N_u$ ,  $E_u$ , and  $g_u$  are the column density, energy, and degeneracy of the upper energy level,  $T_\ell$  and  $T_u$  are the limits of the temperature distribution,  $N_{\text{tot}}$  is the total column density of  $\text{H}_2$ ,  $Z(T)$  is the partition function of the  $\text{H}_2$ , and  $n$  is a generic power-law index that sets the temperature distribution. We set  $T_u = 2000$  K following [Togi & Smith \(2016\)](#) and allow  $N_{\text{tot}}$ ,  $n$ , and  $T_\ell$  to vary.

We have 2 goals with this analysis: 1) Obtain “intrinsic”  $S(4)/S(3)$  line ratios so that we may reconstruct the optical depth of the emission lines in the host galaxy; and 2) Obtain an estimate for the total molecular gas mass and how this gas is distributed spatially. For the first goal, we take the  $\text{H}_2$  line fluxes from our first iteration fits and mask the  $S(3)$  line. Once we obtain a modeled value for the  $S(3)$  line, we can compute the



**Figure 4.** Left: An excitation diagram of the H<sub>2</sub> rotational lines integrated over the full channel 2 FOV. The abscissa is the energy of the upper level of the transition in Kelvin,  $E_u/k$ , and the ordinate is the column density of the upper level of the transition in  $\text{cm}^{-2}$ ,  $N_u$ , normalized by the degeneracy  $g_u$ . The black points show the observed values, with each H<sub>2</sub> line labeled accordingly, and the red line shows the best-fit continuous temperature model, with a  $\chi^2 = 1.52$ . Right: A map of the total molecular gas mass over the channel 2 FOV, obtained by fitting a continuous temperature model to the H<sub>2</sub> excitation diagram, extrapolating to lower temperatures, and integrating over temperature. Note that the color scale is logarithmic (base 10).



**Figure 5.** Maps of the 7.7  $\mu\text{m}$  and 11.3  $\mu\text{m}$  PAH features over the channel 2 FOV.

inferred line ratio as

$$\frac{F_i}{F_j} = \frac{N_i \lambda_j A_i}{N_j \lambda_i A_j} \quad (3)$$

where  $F_i$ ,  $N_i$ ,  $\lambda_i$ , and  $A_i$  are the fluxes, column densities, wavelengths, and Einstein  $A$  coefficients of each line. We then compare this with the observed line ratio to compute an optical depth as described in §3.1.1. After obtaining the optical depth map, we use line fluxes from our second iteration fits, including the  $S(3)$  line, to

obtain estimates for the molecular gas mass. Note that we use the *total* flux of the H<sub>2</sub> lines in both of these procedures, recombining the components from the QSO PSF and host galaxy decomposition. The decomposition into these two components is still important, however, since they may be extinguished by different amounts (this is only relevant for the  $S(3)$  line, so it is not an important distinction for the first goal). Note that including



the rotational lines up to  $S(8)$  limits us to the channel 2 FOV.

We show the excitation diagram for the  $H_2$  rotational lines, integrated over the whole FOV of channel 2, in the left panel of Figure 4. The errors here have been obtained by bootstrapping the spectral fits 100 times, so they are purely statistical. The data are well fit by a temperature distribution with a power law index of  $n = 4.8 \pm 0.1$  and a lower temperature limit of  $T_\ell = 250_{-90}^{+60}$  K. We see that in general these rotational  $H_2$  lines are only sensitive to warm molecular gas at temperatures  $\gtrsim$  a few 100 K. However, the continuous temperature model allows us to extrapolate to lower temperatures and get an estimate of the total molecular gas mass. We use a lower temperature extrapolation value appropriate for ULIRGs and LIRGs of  $T_{\text{ext}} = 80$  K (Togi & Smith 2016), which yields a total molecular gas mass of  $M_{H_2} = 2.2_{-0.1}^{+0.4} \times 10^{10} M_\odot$ . This is in excellent agreement with previous measurements from McDonald et al. (2014) and Russell et al. (2017), who obtained an  $H_2$  mass of  $2.1 \pm 0.3 \times 10^{10} M_\odot$  using a CO-to- $H_2$  conversion factor  $X_{CO} = 0.4 \times 10^{20} \text{ cm}^{-2} (\text{K km s}^{-1})^{-1}$ , equivalent to  $\alpha_{CO} = 0.86 M_\odot \text{ pc}^{-2} (\text{K km s}^{-1})^{-1}$ .

By comparing their  $H_2$  mass measurement to ours, assuming the same underlying CO mass, we can obtain an estimate of the CO-to- $H_2$  conversion factor of  $\alpha_{CO} = 0.9 \pm 0.2 M_\odot \text{ pc}^{-2} (\text{K km s}^{-1})^{-1}$ . This is roughly a factor of 5 smaller than the standard Milky Way disk value of  $\alpha_{CO, \text{Gal}} = 4.3 M_\odot \text{ pc}^{-2} (\text{K km s}^{-1})^{-1}$  (Bolatto et al. 2013). Lower values of  $\alpha_{CO}$  are common in mergers, ULIRGs, and starburst galaxies because these systems tend to have more turbulence and gas inflows which lead to molecular gas at higher temperatures and densities. This increases the molecular gas luminosity per unit mass, lowering  $\alpha_{CO}$  (Togi & Smith 2016; Downes et al. 1993; Downes & Solomon 1998). The extreme cooling and star formation in Phoenix make it comparable to these systems and is the most likely explanation behind the lowered  $\alpha_{CO}$  value. Variations in metallicity can also produce differences in the conversion between CO and  $H_2$ , and are likely the reason that our  $H_2$  mass measurement does not match exactly with Russell et al. (2017) (aside from pure statistical variations).

We also do spaxel-by-spaxel fits of these models, obtaining a molecular gas mass in each spaxel. The corresponding map is shown in the right panel of Figure 4. The mass distribution generally follows the same morphology as the surface brightness.

### 3.1.4. PAH Features

Due to a rather unfortunate alignment in the wavelength boundaries between channels of the MIRI instru-

ment, at the redshift of the Phoenix cluster, the prominent PAH features at  $7.7 \mu\text{m}$  and  $11.3 \mu\text{m}$  both land at the edges between channels 2/3 and 3/4, meaning they are partially cut off in each channel. This motivated us to, in addition to our single-channel fits, also run a multi-channel fit by combining data from channels 2–4, projecting everything onto the channel 2 grid. This way, we are able to measure the full integrated fluxes of these PAH features.

Maps of the total flux of the  $7.7 \mu\text{m}$  and  $11.3 \mu\text{m}$  PAH complexes are shown in Figure 5. The PAH emission is more centrally concentrated than the molecular gas and does not have distinct filaments extending to the south and southeast, but it does have protrusions from the nucleus that generally align with the directions of the filaments. It is clearly extended to both the north and the south, whereas the warm/hot ionized gas phases at  $\sim 10^{5.5}$  K are only extended to the north (see i.e. R25). Qualitatively speaking, then, the PAHs more closely resemble the morphologies of the colder gas phases. The physical extent of the PAHs is likely constrained by the necessity for them to be shielded from hard ionizing UV and X-ray photons from the AGN, and photons and suprathermal electrons from the hot ICM. It is interesting, then, that we still see significant PAH emission even in the centralmost spaxel closest to the X-ray-luminous AGN. This emission likely comes from dusty gas clumps in and around the torus and in the surrounding regions that have lines of sight to the AGN that are shielded by the torus.

### 3.2. Stellar Populations and a Robust SFR

With these new *JWST* data in the MIR, we obtain valuable constraints on the shape of Phoenix’s SED in a region that is dominated by the AGN and thermal dust emission. As such, we calculate the integrated flux within each subchannel (using a consistently sized aperture, which takes up the full FOV of channel 1) and create simulated broadband photometry measurements. We combine these measurements with archival broadband data spanning from the UV to the radio (GALEX, HST, 2MASS, WISE, Herschel/PACS, & Herschel/SPIRE: McDonald et al. (2012); ATCA & SUMSS: McDonald et al. (2014)) and fit SED models using the CIGALE software (Boquien et al. 2019; Yang et al. 2020)<sup>5</sup>. The modules used and parameter space searched are detailed in Table 1. The full range of parameters we wished to search was large enough that doing a sim-

<sup>5</sup> CIGALE website

**Table 1.** CIGALE Parameters

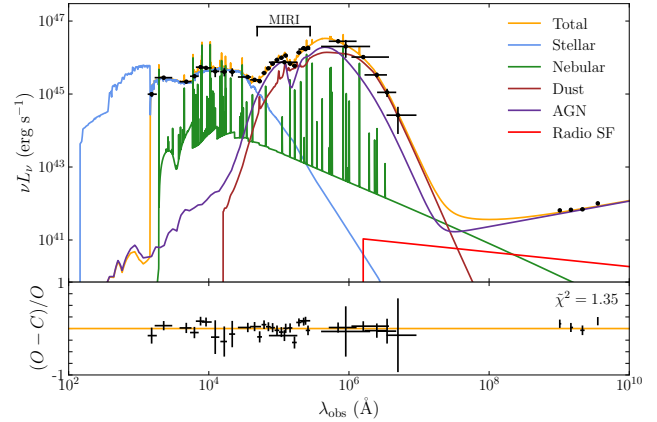
Parameter Description	Name	Searched Values	Bayesian fit value
Star Formation History	<b>sfhdelayed</b>		
Main population e-folding time	<b>tau_main</b>	100, 500, 1000, 2000, 4000, 6000, 8000 Myr	$6000 \pm 2000$ Myr
Main population age	<b>age_main</b>	8000 Myr	
Burst population e-folding time	<b>tau_burst</b>	1, 10, 100, 1000 Myr	$600 \pm 400$ Myr
Burst population age	<b>age_burst</b>	1, 5, 10, 20, 50, 100 Myr	$26 \pm 13$ Myr
Burst population mass fraction	<b>f_burst</b>	0, 0.0001, 0.0005, 0.001, 0.005, 0.01	$0.006 \pm 0.002$
Stellar Populations	<b>bc03</b>		
Initial Mass Function	<b>imf</b>	Salpeter	
Stellar metallicity	<b>metallicity</b>	0.0004, 0.004, 0.008	$0.006 \pm 0.002$
Old & young population separation age	<b>separation_age</b>	10 Myr	
Nebular Emission	<b>nebular</b>		
Ionization parameter	<b>logU</b>	-3	
Gas metallicity	<b>zgas</b>	0.005	
Electron density	<b>ne</b>	$1000 \text{ cm}^{-3}$	
Lyman continuum dust absorption fraction	<b>f_dust</b>	0, 0.001, 0.01, 0.1	$0.01 \pm 0.02$
Line width	<b>lines_width</b>	$800 \text{ km s}^{-1}$	
Dust Attenuation	<b>dustatt_modified_starburst</b>		
Gas reddening	<b>E.BV_lines</b>	0.1, 0.2, 0.3, 0.4, 0.5, 0.6, 0.7	$0.500 \pm 0.002$
Stellar reddening reduction factor	<b>E.BV_factor</b>	0.44	
UV bump amplitude	<b>uv_bump_amplitude</b>	0	
Attenuation curve power law slope modifier	<b>powerlaw_slope</b>	0	
Dust Emission	<b>dl2014</b>		
PAH mass fraction	<b>q_pah</b>	0.47	
Minimum radiation field	<b>umin</b>	10	
Power law slope	<b>alpha</b>	2	
Illumination fraction	<b>gamma</b>	0.25	
AGN	<b>skirtor2016</b>		
Average edge-on optical depth at $9.7 \mu\text{m}$	<b>t</b>	9	
Dust density radial slope	<b>pl</b>	1	
Dust density polar slope	<b>q</b>	0	
Torus opening angle	<b>oa</b>	$50^\circ$	
Ratio of outer to inner radius	<b>R</b>	30	
Inclination angle	<b>i</b>	60, 70, 80, $90^\circ$	$80 \pm 1^\circ$
Optical disk power law slope modifier	<b>delta</b>	1.0	
AGN fraction of IR luminosity	<b>fracAGN</b>	0, 0.1, 0.2, 0.3, 0.4, 0.5, 0.6, 0.7, 0.8, 0.9, 0.99	$0.50 \pm 0.01$
Polar dust extinction	<b>EBV</b>	0, 0.2, 0.4	$0.21 \pm 0.05$
Radio emission	<b>radio</b>		
FIR/radio correlation coefficient	<b>qir_sf</b>	2.7	
Star formation synchrotron slope	<b>alpha_sf</b>	0	
AGN radio loudness	<b>R_agn</b>	0.1, 1, 10, 100, 1000	10
AGN radio emission slope	<b>alpha_agn</b>	1.35	

**Note:** Any parameters not listed here take their default values.

gle run varying everything at the same time would have been computationally infeasible. As such, we took an iterative approach and varied parameters in groups. The values shown in Table 1 for the nebular, dust, AGN, and radio modules that are fixed have been selected from previous iterations. During these iterations, the other parameters are given values based on educated guesses of the conditions in Phoenix A—for example, given that it hosts a bright type II AGN, we assumed an inclination angle of  $70^\circ$  and an AGN fraction of 50%. In most cases, we see that the final values of these parameters in our final fits are not too far from these initial guesses. The new *JWST* points in the MIR provide stronger constraints on the shape of the AGN and dust emission, allowing us to adjust many of the AGN torus parameters from their default values. However, a major strength of CIGALE comes from its ability to constrain parameters in different wavelength bands using the principles of energy balancing and correlations between parameters from the underlying physics. This is why, in our final iteration, we still allowed certain parameters in these modules to vary from their previously found values, such as the AGN fraction and radio loudness.

A notable caveat to this analysis is the spatially agnostic nature of the CIGALE fit, which presents itself most prominently in the decomposition between the “dust emission” and “AGN” components of the model. The templates CIGALE uses for dust emission only consider starlight-heated dust, whereas a powerful AGN such as the one in Phoenix may also contribute to heating the dust all throughout the host galaxy. In contrast, the SKIRTOR AGN templates only consider the radiative transfer process through the dust in the nucleus/torus region, not throughout the whole galaxy. A study from [Viaene et al. \(2020\)](#) looking at NGC 1068 showed, using their own radiative transfer analysis, that considering the effects of the AGN separately caused it to contribute up to 15% of the total dust heating, depending on viewing angle. In the case of Phoenix, with a much more luminous AGN, this fraction could be even higher. Nevertheless, we expect the ramifications of this on our interpretation of the results to be minor: [Viaene et al. \(2020\)](#) performed comparison CIGALE fits and found the SFRs to be in agreement with their models. Without the inclusion of an AGN component, they found the young stellar populations to be overly attenuated in order to boost the MIR dust emission to the observed levels, but in our case the separate inclusion of an AGN component with a distinct shape in the MIR likely alleviates this concern.

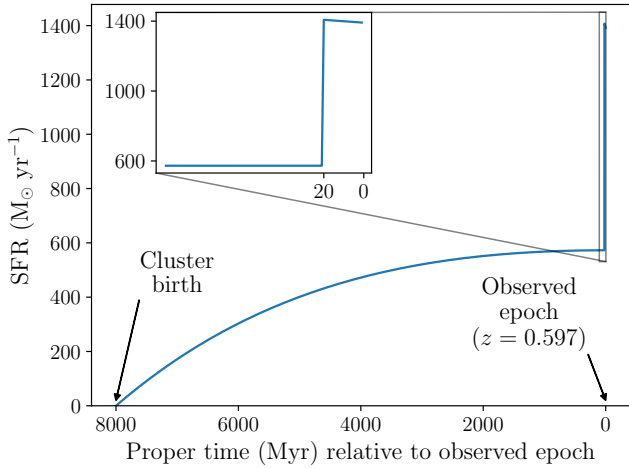
The final SED model is shown in Figure 6. The attenuated stellar populations (blue) dominate in the UV



**Figure 6.** The best-fit SED model for Phoenix A. Photometry data points are shown in black with error bars. The full SED model spectrum is the amber line, and the individual components of the SED are labeled in the legend. The bottom panel shows the residuals of the fit.

and optical due to the obscuration of the AGN, while the AGN (purple) and dust emission (brown) dominate in the MIR-FIR. The data from  $\sim 5 - 10 \mu\text{m}$  in the observed frame (MIRI channel 1 and 2) provide the strongest constraints on the relative power of the AGN and dust emission, since dust emission in this range would correspond to dust heated above  $\gtrsim 300 \text{ K}$ , which is difficult to achieve without the presence of an AGN. Notice that the AGN component dominates the SED in this range, whereas the dust emission becomes the dominant component in the FIR above  $\sim 100 \mu\text{m}$ , corresponding to much colder ( $\sim 30 \text{ K}$ ) temperatures. Interpolating our model at a rest-frame wavelength of  $24 \mu\text{m}$  gives a total luminosity of  $\nu L_\nu(24 \mu\text{m}) \approx 3.0 \times 10^{46} \text{ erg s}^{-1}$  and an AGN-subtracted (i.e. host galaxy) luminosity of  $\approx 1.3 \times 10^{46} \text{ erg s}^{-1}$ . We will use these values in the next section for a more in-depth analysis of the heating mechanisms of the different gas and dust phases.

The star formation history is shown in Figure 7. The models settle on a fairly consistent star formation rate throughout the past 8 Gyr of the galaxy’s history, with the average SFR over all time being around  $400 M_\odot \text{ yr}^{-1}$ . The recent burst of star formation started  $26 \pm 13 \text{ Myr}$  ago and favors models with large  $e$ -folding times of  $600 \pm 400 \text{ Myr}$ , bringing the current instantaneous value of the SFR well above  $1000 M_\odot \text{ yr}^{-1}$ . In other words, the star formation remains fairly constant after the burst, rather than dipping back down to the pre-burst rate. This implies that even the youngest O-type stars with lifetimes  $\leq 10 \text{ Myr}$  should be present in the galaxy. The presence of extremely luminous O-type stars perhaps explains why, despite the young population contributing a considerable amount to the observed



**Figure 7.** The star formation rate is shown as a function of time in Phoenix’s rest frame, relative to the observed epoch. As the main “old” stellar population has an age fixed at 8 Gyr, the furthest back the plot goes is 8 Gyr relative to the observed epoch (corresponding roughly to the Big Bang). An inset is shown zooming in on the most recent 100 Myr of star formation, showing the rapid spike at 20 Myr.

**Table 2.** CIGALE Stellar Population Parameters

Parameter	Symbol	Value
Old population age	$t_{*,old}$	8 Gyr
Young population age	$t_{*,young}$	$26 \pm 13$ Myr
Old population mass <sup>†</sup>	$M_{*,old}$	$2.6 \pm 0.5 \times 10^{12} M_{\odot}$
Young population mass <sup>†</sup>	$M_{*,young}$	$1.3 \pm 0.1 \times 10^{10} M_{\odot}$
Stellar metallicity	$Z_*$	$0.006 \pm 0.002$
Instantaneous SFR <sup>‡</sup>	SFR	$1330 \pm 130 M_{\odot} \text{ yr}^{-1}$
10 Myr averaged SFR <sup>‡</sup>	$\langle \text{SFR} \rangle_{10}$	$1340 \pm 100 M_{\odot} \text{ yr}^{-1}$
100 Myr averaged SFR <sup>‡</sup>	$\langle \text{SFR} \rangle_{100}$	$740 \pm 80 M_{\odot} \text{ yr}^{-1}$

All measured stellar masses and SFRs assume a Salpeter IMF.

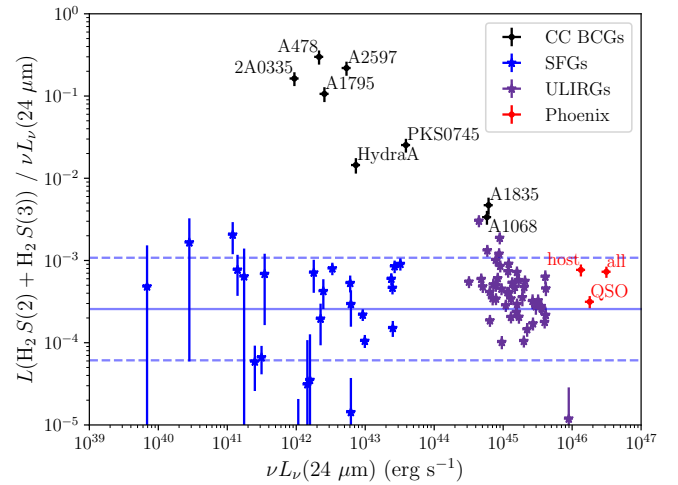
<sup>†</sup>To convert stellar masses to those that would be measured with other IMFs, multiply by 0.61 (Chabrier) or 0.66 (Kroupa) (Madau & Dickinson 2014).

<sup>‡</sup>To convert SFRs to those that would be measured with other IMFs, multiply by 0.63 (Chabrier) or 0.67 (Kroupa) (Madau & Dickinson 2014).

optical/UV luminosity, it only contributes  $\sim 0.5\%$  of the total stellar mass. The stellar populations and star formation rates are summarized in Table 2. These values are derived from the star formation history model given by the parameters in Table 1.

### 3.3. Scaling Relations

D11 studied a sample of cool core (CC) BCGs and found that the thermal dust continuum and PAH fea-



**Figure 8.** The ratio of the combined  $H_2$  0–0  $S(2)$  and  $S(3)$  luminosity over the  $24 \mu\text{m}$  continuum luminosity  $\nu L_{\nu}(24 \mu\text{m})$  plotted as a function of  $\nu L_{\nu}(24 \mu\text{m})$ . The black points show the cool core (CC) BCGs from the D11 sample, and the red points show the Phoenix cluster: “all” corresponds to the integrated values over the whole field of view, “host” corresponds to the integrated values after the QSO PSF has been subtracted, and “QSO” corresponds to the integrated QSO PSF values. The blue stars show galaxies from the SINGS sample designated as “H II” or star-forming galaxies (SFGs) by Smith et al. (2007). The solid blue line shows the average value of these galaxies, and the dashed blue lines show the 1- $\sigma$  standard deviation. The purple stars show ULIRGs from Farrah et al. (2007).

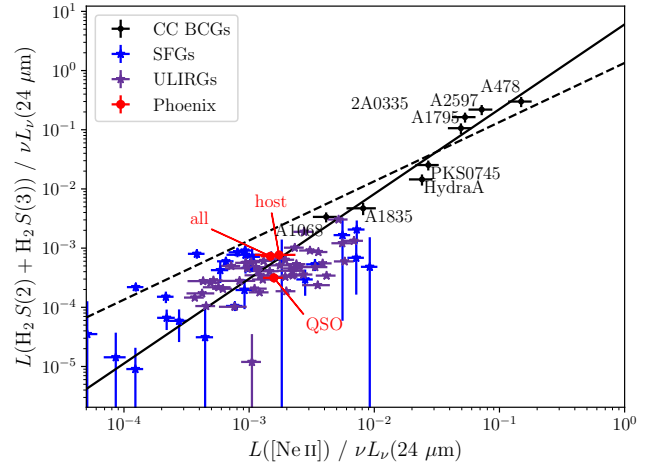
tures were consistent with being heated primarily by star formation, whereas the warm molecular  $H_2$  gas and ionized [Ne II] gas had an additional heating source, which they attributed to energetic particles from the ICM. It is useful to reexamine some of these correlations with the Phoenix cluster in mind, for a few reasons: (1) To understand the relative contributions of different heating sources in Phoenix itself, and compare them to the typical cool core population; (2) To isolate the effects of AGN photoionization heating, since none of the BCGs studied in the D11 sample exhibited evidence of AGN activity; and (3) To identify the relative importances of different heating sources in offsetting cooling flows.

#### 3.3.1. Rotational $H_2$ Line Correlations

Being the gas phase most closely linked to star formation, cold molecular gas is an important tool in studying the characteristics of star-forming regions. However, it is often difficult to detect directly, as cold molecular  $H_2$  does not emit strongly, and must be traced by the second most abundant molecule in the ISM (CO) instead. Warm molecular gas heated to a few 100 K, on the other hand, has rovibrational emission lines in the infrared that can be used to directly detect the warm

H<sub>2</sub> gas, but no longer has the direct connection to star formation due to its increased excitation. Untangling how much of this emission is due to star formation, as opposed to other sources, can be an important clue in distinguishing Phoenix from other BCGs. In the D11 sample of BCGs, the ratio of the combined luminosity of the H<sub>2</sub> 0–0 *S*(2) and *S*(3) lines ( $L_{\text{H}_2}$ ) and the 24  $\mu\text{m}$  continuum luminosity ( $L_{24} \equiv \nu L_\nu$  at 24  $\mu\text{m}$ ) was elevated orders of magnitude above typical values seen in starburst galaxies (Treyer et al. 2010) (from  $\sim 4 \times 10^{-4}$  to as high as 0.3), suggesting that star formation is not a significant heating mechanism, and other energy sources, such as cosmic rays, likely play an important role in the observed H<sub>2</sub> luminosities. However, the massive starburst in the Phoenix cluster gives it the unique position of having emission components comparable to both the BCGs and the star-forming galaxies.

In order to make this comparison, we need a measurement of  $L_{24}$  for Phoenix. For this, we take the values interpolated from our CIGALE fit in §3.2. Indeed, on average we see a much smaller  $L_{\text{H}_2}/L_{24}$  ratio of  $\sim 8 \times 10^{-4}$ . It lies along the anticorrelation between  $L_{\text{H}_2}/L_{24}$  and  $L_{24}$  noted by D11, which is primarily due to its increased  $L_{24}$  relative to the other BCGs. We recreate Figure 10b from D11 in Figure 8, which shows this anticorrelation. We compare the BCG sample to a sample of nearby infrared-luminous galaxies: the Spitzer Infrared Nearby Galaxies Survey (SINGS), with photometry measurements taken from Dale et al. (2007), H<sub>2</sub> measurements taken from Roussel et al. (2007), and PAH and Neon line measurements taken from Smith et al. (2007). We select only the star-forming galaxies (SFGs), designated by the type “H II” by Smith et al. (2007), and show this sample with blue stars in Figure 8. These galaxies have  $L_{\text{H}_2}/L_{24}$  ratios much smaller than the BCGs and more similar to Phoenix, but with smaller overall  $L_{24}$ . We also include a selection of Ultraluminous Infrared Galaxies (ULIRGs) from Farrah et al. (2007). Powered by vigorous starbursts or AGNs, the ULIRGs bridge the gap between the normal star-forming galaxies and Phoenix. This shows that Phoenix is an extension of this population into the cluster environment—a unique case where a galaxy in the highest mass regime hosts both a QSO and a starburst. This would seem to imply that the majority of the H<sub>2</sub> emission in Phoenix is produced by stellar heating, which would make it unique among the cool core BCGs. Note that the presence of the AGN increases  $L_{24}$  substantially above that produced by dust-reprocessed stellar light in the host galaxy. We have attempted to account for this by subtracting the portion of  $L_{24}$  generated by the AGN and recovering the  $L_{24}$  just from the host galaxy. But as discussed in §3.2,



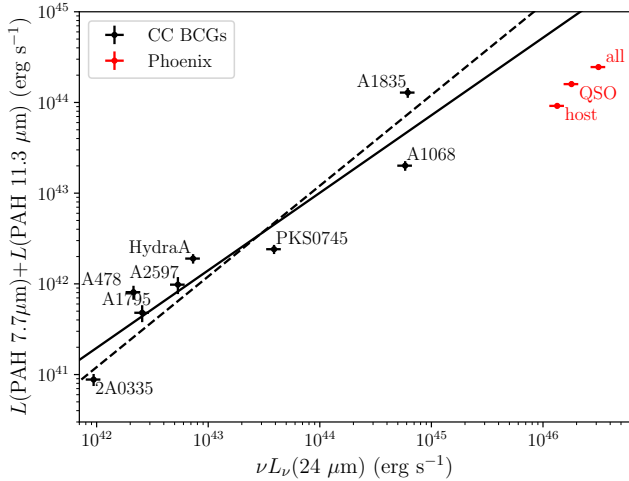
**Figure 9.** The ratio of the combined H<sub>2</sub> 0–0 *S*(2) and *S*(3) luminosity over the 24  $\mu\text{m}$  continuum luminosity  $\nu L_\nu(24 \mu\text{m})$  versus the ratio of the [Ne II]  $\lambda 12.813 \mu\text{m}$  luminosity over  $\nu L_\nu(24 \mu\text{m})$ . Both luminosities are normalized to  $\nu L_\nu(24 \mu\text{m})$  to remove any “bigger is bigger” effects (Kennicutt 1990). The data points are labeled identically to Figure 8. The dashed line shows a 1:1 correlation, and the solid line shows the best-fit power law, which is marginally steeper.

if the AGN is a significant source of heating for the dust in the host galaxy and not just the nucleus, this may not be properly separated by our decomposition. Nevertheless, even if the true  $L_{24}$  value from just starlight is a few times smaller than the “host” value, Phoenix would still land safely below the two next-most-starburst-like BCGs, Abell 1068 and 1835.

We also see a strong correlation between the H<sub>2</sub> luminosity and the [Ne II]  $\lambda 12.813 \mu\text{m}$  luminosity ( $L_{[\text{Ne II}]}$ ), corroborating that found in D11 (their Figure 11, our Figure 9). Phoenix lies right along the best-fit power law,  $(L_{\text{H}_2}/L_{24}) \propto (L_{[\text{Ne II}]} / L_{24})^{1.4 \pm 0.1}$ , but lands in a region of parameter space similar to the SINGS star-forming galaxies and ULIRGs as opposed to the other BCGs. This correlation means that the heating sources for the molecular gas and the warm ionized gas must be tightly interlinked. In other words, if the H<sub>2</sub> excitation is predominantly due to star formation, as it seems to be based on the  $L_{\text{H}_2}/L_{24}$  ratio, then the [Ne II] excitation is likely also primarily due to star formation.

### 3.3.2. PAH Feature Correlations

The PAH features are emitted by bending and stretching modes of the bonds between carbon and hydrogen atoms in very small dust grains (Leger & Puget 1984; Boulanger et al. 1998; Van Kerckhoven et al. 2000)—these modes can be excited by the absorption of UV photons (Allamandola et al. 1985; Sloan et al. 1999), making PAH emission a strong tracer of the stellar ion-



**Figure 10.** The combined 7.7  $\mu\text{m}$  and 11.3  $\mu\text{m}$  PAH luminosity as a function of the 24  $\mu\text{m}$  continuum luminosity. The ensemble value for Phoenix is plotted against the D11 sample of BCGs. The solid line shows the best-fit power law, and the dashed line shows a slope of 1.

ization field (Peeters et al. 2004; Brandl et al. 2006; Förster Schreiber et al. 2004). Thus, in typical star-forming galaxies where the IR continuum is primarily a result of reprocessed stellar light by larger dust grains, the PAH and continuum luminosity are observed to be strongly correlated with each other (Wu et al. 2010). D11 found that such a correlation also exists in their sample of cool core BCGs, indicating that starlight is still the main contributor to the observed PAH luminosities, even in massive elliptical galaxies. We plot this relationship, recreating D11’s Figure 8a, in Figure 10. Phoenix noticeably falls below the trend seen in the other BCGs, even after subtracting the QSO PSF, by 2.5–3 $\sigma$  (where  $\sigma$  here is the scatter in the  $L_{24}$ - $L_{\text{PAH}}$  relation). This may be due to PAH emission being suppressed by the presence of the AGN, as has been shown to be the case in numerous studies (Roche et al. 1991; Xie & Ho 2022). Hard ionizing radiation, such as from an AGN, can destroy PAH grains and thus may have an effect on the PAH grain size distribution and ionization fraction. This radiation can also come from the hot ICM in a cluster environment, leading D11 to conclude that the IR-emitting PAHs seen in BCGs must be somehow shielded from the hot gas, perhaps through a layer of dusty gas with larger dust grains. Additionally, Phoenix’s powerful AGN is heavily dust obscured, leading to the potential for localized pockets where PAHs can exist, shielded from both the AGN and the ICM.

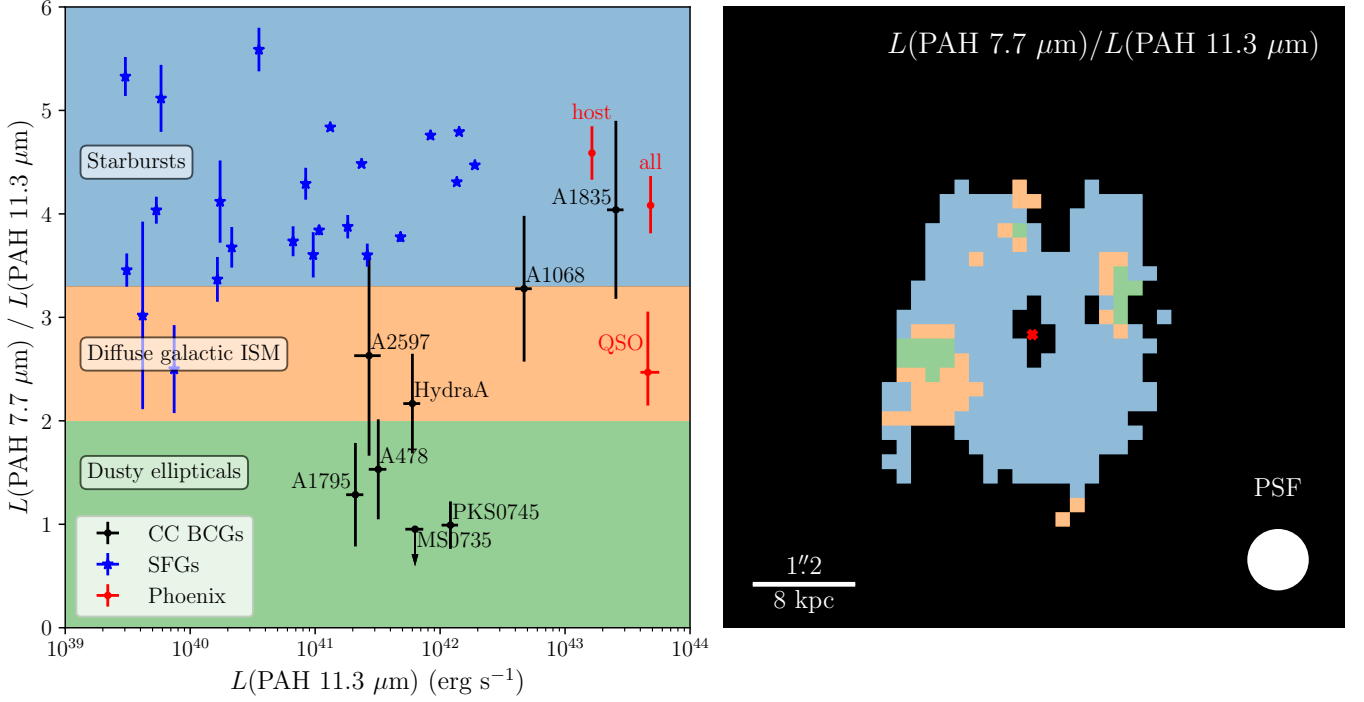
We can further constrain the ionization source by considering the ratio of the 7.7  $\mu\text{m}$  to 11.3  $\mu\text{m}$  PAH features,  $L_{7.7}/L_{11.3}$ , which is sensitive primarily to the fraction

of ionized and neutral PAHs in the system (Draine & Li 2007). Starburst systems with a large population of young, hot stars and a hard radiation field typically having elevated ratios of  $\sim 3$ –7 (Smith et al. 2007). The diffuse galactic ISM, with more evolved stars and an intermediate radiation field, has ratios between 2–3.3 (Sakon et al. 2004). Finally, dusty elliptical galaxies, with only evolved stars and a soft radiation field, typically have much lower ratios between 1–2 (Kaneda et al. 2008). We examine  $L_{7.7}/L_{11.3}$  in each spaxel and classify them into 3 categories, for simplicity: starbursts (young stars;  $L_{7.7}/L_{11.3} > 3.3$ ), diffuse galactic ISM (middle-aged stars;  $2 < L_{7.7}/L_{11.3} < 3.3$ ), and dusty ellipticals (old stars;  $L_{7.7}/L_{11.3} < 2$ ). The results are shown in Figure 11. Compared with the D11 sample and the SINGS sample, we see that most of Phoenix A’s host galaxy has ratios typical of starburst galaxies. However, there are a few pockets to the southeast and northwest of the nucleus where the ratio drops all the way into dusty elliptical territory. This may indicate that the cooling flow is more suppressed in these regions compared to their surroundings, preventing younger stars from forming and causing the primary ionization source to be old stars. Alternatively, these regions may have a higher dust obscuration around the young stars, but we do not see any coincidence between the pockets of low PAH ratios here and regions of enhanced dust obscuration in Figure 2. The ratio also drops significantly in the nucleus (as shown by the “QSO” data point), following the trends seen in Smith et al. (2007) for AGN-dominated systems. AGN feedback is likely preventing new stars from forming within  $\sim 1$  kpc from the SMBH—at this scale, the closer to the SMBH, the more effective heating becomes. This has been observed in simulations with substantial rises in the innermost entropy and turbulence (e.g. Wittor & Gaspari 2020).

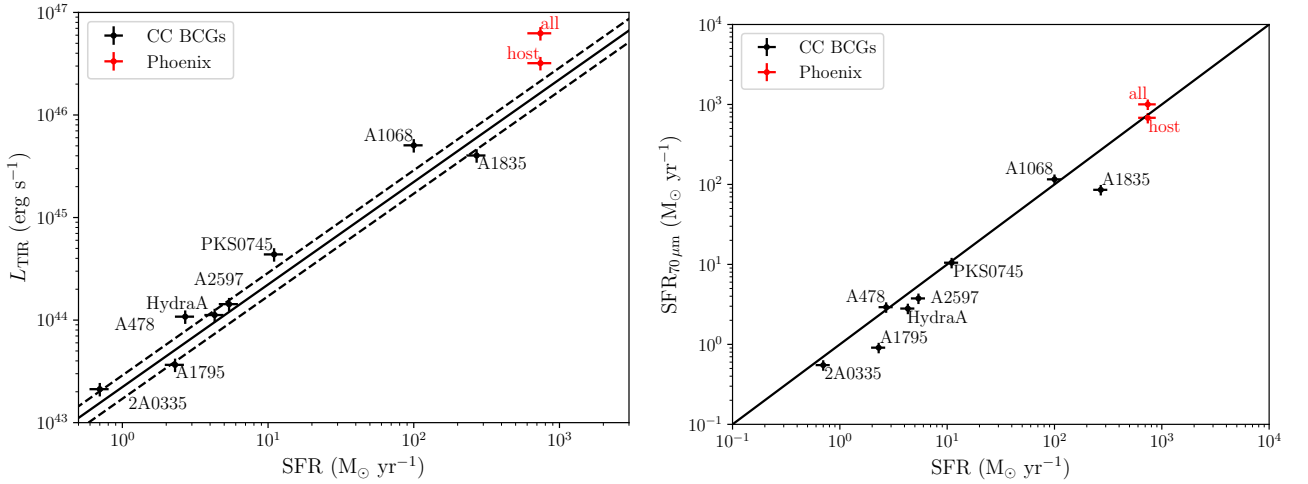
### 3.3.3. SFR Correlations

The literature has many calibrated star formation rate correlations with host galaxy properties, including integrated continuum luminosities, single-band continuum luminosities, and emission line luminosities. These correlations are applicable only in certain circumstances, so they can be compared and taken advantage of to infer whether these conditions hold. Here, we analyze SFRs from a number of different indicators in comparison to our modeled SFR from the SED (§3.2), which we take to be the “true” (read: most accurate) value.

Firstly, the SFR can be estimated from the total infrared luminosity  $L_{\text{TIR}}$  (integrated from 5–1000  $\mu\text{m}$ ) using Kennicutt (1998), and the 70  $\mu\text{m}$  luminosity  $L_{70} \equiv \nu L_{\nu}(70 \mu\text{m})$  using Calzetti et al. (2010). We recreate



**Figure 11.** *Left:* The ratio of the 7.7  $\mu\text{m}$  PAH luminosity over the 11.3  $\mu\text{m}$  PAH luminosity as a function of the 11.3  $\mu\text{m}$  PAH luminosity. Different regions are colored according to the dominant ionization mechanisms expected to produce PAH ratios in this regime: starbursts (blue), diffuse galactic ISM (orange), and dusty ellipticals (green). The D11 sample is plotted in black, Phoenix is shown in red, and the SINGS star-forming galaxies are shown in blue. The data points are labeled identically to Figure 8. *Right:* A 2D map of the PAH luminosity ratio in each spaxel. Only spaxels where both PAHs are detected with an  $S/N \geq 1$  are shown. The spaxels are colored according to which region they fall in on the left panel. A scale bar with physical and angular units is shown in the bottom left, and a circle displaying the size of the PSF FWHM is shown in the bottom right.



**Figure 12.** *Left:* The total infrared luminosity  $L_{\text{TIR}}$  integrated from 5–1000  $\mu\text{m}$ , as a function of the modeled SFR. The solid line shows the Kennicutt (1998) relation, and the dashed lines show a 30% scatter on that relation. *Right:* The SFR estimated from the monochromatic 70  $\mu\text{m}$  luminosity as a function of the modeled SFR. The solid line shows the Calzetti et al. (2010) relation.

D11’s Figure 4 in Figure 12, showing both of these correlations for Phoenix, using  $L_{\text{TIR}}$  and  $L_{70}$  obtained from the SED fitting. We notice that the  $L_{\text{TIR}}$  correlation in particular would vastly overpredict the SFR at  $> 2000 M_{\odot} \text{ yr}^{-1}$  if no AGN correction is accounted for. However, it lines up fairly well after subtracting the AGN contribution. These discrepancies confirm, as we saw in the SED modeling, that the AGN, despite being heavily obscured in the optical, accounts for a significant fraction of the underlying continuum luminosity throughout the whole infrared range. This includes contributions directly from the accretion disk itself, those which get absorbed and re-emitted by dust in the torus and the polar regions, and synchrotron emission (at longer wavelengths) from the bipolar radio jets.

The SFR can also be measured from the [Ne II] and [Ne III] lines (Ho & Keto 2007). Following D11, we take  $\text{Ne}^+/\text{Ne} = 0.75$  and  $\text{Ne}^{2+}/\text{Ne} = 0.15$ . We recreate their Figure 12 in Figure 13 (left). We include the sample of star-forming galaxies used by Xie & Ho (2019) as a reference point—for these galaxies, “SFR<sub>model</sub>” refers to SFRs obtained from the MPA/JHU catalogue<sup>6</sup>. After properly subtracting the contribution to the [Ne II] and [Ne III] lines from AGN photoionization, we see that the “host” point lies close to the expected value for SFGs (solid line)—the [Ne II] and [Ne III] are only marginally overluminous compared to the average SFG, confirming that stellar and AGN photoionization combined make up the vast bulk of the observed luminosities of these lines. Unfortunately, we cannot compare with the H<sub>2</sub>-calibrated SFR since it relies on the  $S(0)$  line, which falls outside of the wavelength coverage of MIRI at Phoenix’s redshift. But considering the strong correlation between the H<sub>2</sub> and [Ne II] luminosities found in §3.3.1, we can infer that we would likely see good agreement with the modeled SFR value here as well.

Additionally, we can look at the SFR inferred from the PAH features, using the relation calibrated by Xie & Ho (2019). For each BCG, we take an average of the SFRs inferred from the 7.7  $\mu\text{m}$  and 11.3  $\mu\text{m}$  PAH features. Comparing these SFRs to the modeled values in Figure 13 (right) shows a systematic deficit, with the PAH-based SFRs being 50–80% lower. In this panel, we also show the Xie & Ho (2019) sample of galaxies, but now split up between blue compact dwarfs (BCDs) in blue and normal galaxies in green. The normal galaxies have a typical PAH-based SFR in agreement with the Ne-based SFR. However, we see a decline in both the BCDs and BCGs by more than an order of magnitude.

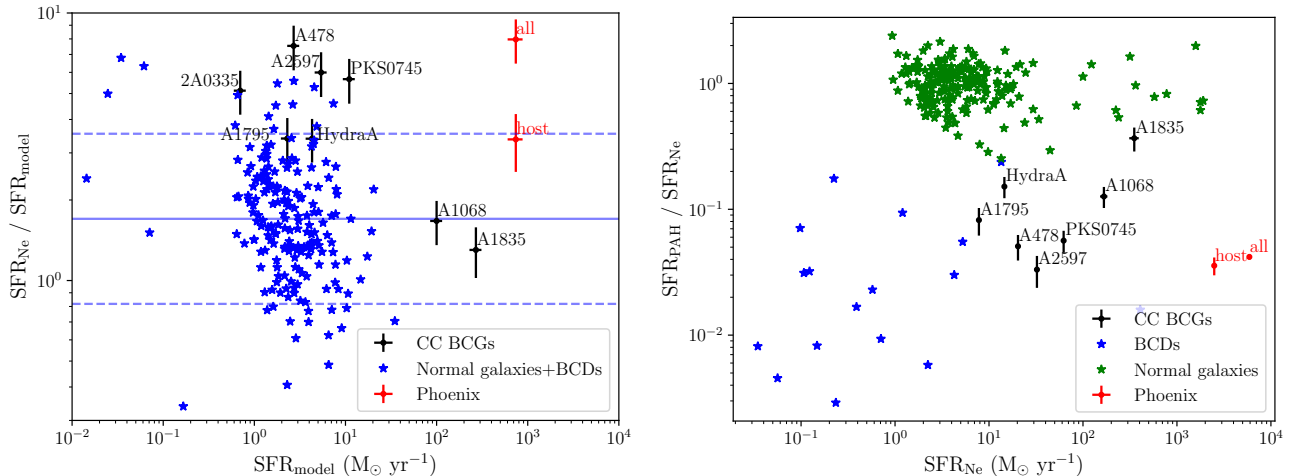
Xie & Ho (2019) address this for the BCD population by adopting a different scaling offset for galaxies with  $M_* < 10^9 M_{\odot}$ —we have not included this correction in the Figure to highlight the apparent PAH deficit in these galaxies and to show the similarities they have with the BCGs. Phoenix, in particular, has a PAH-based SFR almost an order of magnitude smaller than its modeled value. This may be evidence for a PAH deficit in the high-mass galaxy population similar to the deficit in the BCDs: the Xie & Ho (2019) relation we utilize is calibrated for the general galaxy population with stellar masses between  $10^9$ – $10^{11.4} M_{\odot}$ , whereas the BCGs we examine here all have stellar masses  $\gtrsim 10^{11} M_{\odot}$ . The cluster environment may have a significant effect on the survivability of PAHs: collisions with high-energy electrons from the ICM (and an AGN, if active) can sputter and destroy the dust grains on extremely short timescales. D11 argue, using the analysis of Micelotta et al. (2010), that PAHs embedded in a 1 keV,  $0.1 \text{ cm}^{-3}$  plasma could not survive longer than a few hundred years. However, dust can also locally enhance cooling, nurturing the formation of cold gas clouds around the dust that act as a protective shield against the energetic electrons and ions in the ICM, allowing the dust to survive longer in these localized cooling regions. Micelotta et al. (2010) estimate that for conditions similar to the Orion nebula (7000 K,  $10^4 \text{ cm}^{-3}$ ), the PAH survivability is much higher, at roughly 10 Myr. The feeding and feedback cycle of the AGN may also play an important role in periodically refreshing the dust content of the ICM by blowing out dust from the nucleus during outbursts and allowing for more dust formation (or, rather, lessened dust sputtering) during periods of inactivity.

#### 4. DISCUSSION: AN UNDERMASSIVE BLACK HOLE?

With the SFRs of order  $\sim 1000 M_{\odot} \text{ yr}^{-1}$  and molecular gas masses of order  $\sim 10^{10} M_{\odot}$  pointing to massive amounts of cooling gas in the Phoenix cluster, the question then becomes: What makes this cluster unique? Why is this cluster able to host a massive cooling flow while every other observed cluster cannot? The simplest explanation is that there is nothing particularly special about the Phoenix cluster, but we just happened to be observing it at a time when it is undergoing a short-lived cooling spike that will not last much longer than  $\sim$ a few Myr (as we proposed in R25). If indeed all clusters undergo this phase of rapid cooling once throughout their lifetimes, then we should expect to see about 1 in every 10,000 clusters (which is roughly the amount of clusters known—e.g. Klein et al. 2024) experiencing such an event. This seems to line up with expectations, but

<sup>6</sup> <https://wwwmpa.mpa-garching.mpg.de/SDSS/DR7/>





**Figure 13.** *Left:* A comparison between the SFR estimated from the [Ne II] and [Ne III] line luminosities and the SFR modeled from the SED. The data points for the BCGs are in black, Phoenix is in red, and Xie & Ho (2019) galaxies are in blue. For Xie & Ho (2019) galaxies, “ $SFR_{\text{model}}$ ” refers to SFRs from the MPA/JHU catalogue. The solid blue line shows the average value of the Xie & Ho (2019) galaxies, while the dashed blue line shows the  $1-\sigma$  standard deviation. *Right:* A comparison between the SFR estimated from the 7.7  $\mu\text{m}$  and 11.3  $\mu\text{m}$  PAH luminosities and the SFR estimated from the [Ne II] and [Ne III] lines. The colors here are the same, except that the Xie & Ho (2019) galaxies are split up into BCDs (in blue) and non-BCDs (in green). The BCDs here do *not* use the different scaling relation parameters for galaxies with  $M_{*} < 10^9 M_{\odot}$  as suggested by Xie & Ho (2019), to highlight the apparent deficit in PAHs in these systems.

it becomes problematic when we consider that clusters should still exhibit post-starburst signatures long after they have experienced these rapid cooling spikes. These features are generally not seen, even in cool core clusters, and are more often associated with other processes such as galaxy interactions, mergers, and ram-pressure stripping (Werle et al. 2022). Therefore, it seems that we can rule out the presupposition that there is *nothing* special at all about the Phoenix cluster.

Another idea, previously explored in McDonald et al. (2018) and McDonald et al. (2019), is that the Phoenix cluster hosts an undermassive SMBH relative to the size of its cool core, which is expected to occur in the most massive galaxy clusters. In this scenario, rapid cooling drives the accretion rate of the AGN to high Eddington ratios ( $\dot{M}/\dot{M}_{\text{Edd}} \lesssim 5\%$ ). But at these higher Eddington ratios, much of the power output of the AGN comes in the form of radiative feedback as opposed to mechanical feedback, which is less effective at suppressing cooling and may even enhance it through the inverse Compton effect close to the AGN (McDonald et al. 2019). Indeed, Russell et al. (2013) showed that mechanical power output tends to become saturated at  $\sim 1\%$  of the Eddington luminosity, while radiative power continues to grow with the accretion rate.

While there are currently only weak constraints on the mass of Phoenix’s black hole, it is confirmed to show signs of both radiative (bright SEDs; §3.2; McDonald et al. 2012) and mechanical (X-ray cavities, radio jets;

Hlavacek-Larrondo et al. 2015; Timmerman et al. 2021) feedback. Estimates of the mechanical power output place it at  $0.5\text{--}1 \times 10^{46} \text{ erg s}^{-1}$  (McDonald et al. 2019), while we can estimate from our SED fitting in §3.2 a radiative power output of  $L_{\text{bol}} = 3 \times 10^{46} \text{ erg s}^{-1}$ . The fact that these are similar in magnitude suggests that the AGN has only recently undergone (or perhaps is still undergoing) a transition in feedback modes (McDonald et al. 2015). In addition, the mechanical power is *just* high enough to balance with the cooling luminosity of  $\sim 10^{46} \text{ erg s}^{-1}$  (McDonald et al. 2019), and it corresponds to the mechanical feedback limit of a  $\sim 10^{10} M_{\odot}$  black hole. If Phoenix’s black hole has only recently experienced a period of rapid growth up to  $10^{10} M_{\odot}$ , this would explain the puzzlingly high rates of cooling despite the black hole’s current power output being seemingly large enough that it should offset this cooling.

As the cluster continues to evolve, in this picture, we should expect the cooling to begin being regulated more efficiently by the recently grown black hole. Now that the mechanical power output has reached levels sufficient to balance cooling, the cooling rates, star formation rates, and accretion rate of the SMBH should all slow down until they reach roughly the percent level of the classical cooling rate. In fact, we can estimate from the bolometric AGN luminosity that the black hole’s current accretion rate is  $\dot{M} = L_{\text{bol}}/\eta c^2 \approx 5 M_{\odot} \text{ yr}^{-1}$  (assuming an efficiency  $\eta = 0.1$ ), which is about an order of magnitude lower than previously thought (due to un-

certain X-ray-to-bolometric luminosity corrections; [McDonald et al. 2012](#)). This may indeed be an indication that the black hole’s growth has now slowed after reaching a mass sufficient to balance cooling. This trend will ultimately drive Phoenix towards Abell 1835 and Abell 1068 on many of our figures, decreasing dramatically in  $L_{24}$  as the AGN radiative power output diminishes, and decreasing less dramatically in other quantities ( $L_{\text{H}_2}$ ,  $L_{[\text{NeII}]}$ ,  $L_{\text{PAH}}$ ). The ratio of the 7.7  $\mu\text{m}$  to 11.3  $\mu\text{m}$  PAH features will also decrease with the SFR, trending towards values more typical of the diffuse galactic ISM. The PAH-derived SFRs, however, will likely stay suppressed relative to other SFR indicators, as this seems to be largely due to the influence of the ICM and is not a feature specific to Phoenix. Whether this scenario holds up in reality would largely be determined with more precise constraints on the SMBH mass.

## 5. CONCLUSION

Since its discovery, the Phoenix Cluster has stood out as a unique system, even among cool core clusters, due to its hosting of the most massive and efficient cooling flow in the known universe ([McDonald et al. 2012](#)). The results of our analysis of the molecular gas, dust, and star formation from MIRI/MRS data have only further exemplified this uniqueness. We list the important results of our analysis, in sequence, below:

1. We have developed a new technique for measuring the optical depth due to silicate absorption in the warm molecular line-emitting gas based on fitting excitation models of the rotational  $\text{H}_2$  lines.
2. Using this technique in conjunction with the LOKI spectral modeling software, we have measured the total molecular gas mass in the Phoenix cluster to be  $2.2_{-0.1}^{+0.4} \times 10^{10} M_{\odot}$ , in agreement with previous estimates made using CO emission. We have estimated the CO-to- $\text{H}_2$  conversion factor to be  $\alpha_{\text{CO}} = 0.63 \pm 0.11 M_{\odot} \text{ pc}^{-2} (\text{K km s}^{-1})^{-1}$ .
3. We have filled in the MIR gap in Phoenix’s SED and obtained refined measurements of the stellar mass,  $M_* = 2.6 \pm 0.5 \times 10^{12} M_{\odot}$ , and star formation rates,  $\langle \text{SFR} \rangle_{10} = 1340 \pm 100 M_{\odot} \text{ yr}^{-1}$  and  $\langle \text{SFR} \rangle_{100} = 740 \pm 80 M_{\odot} \text{ yr}^{-1}$ , in agreement within  $\pm 1\sigma$  of previous estimates based on a number of different scaling relations ([McDonald et al. 2012](#)).
4. We have found, using correlations between different MIR emission features, that star formation—and in particular young, hot stars formed via the cooling flow—in the Phoenix Cluster’s BCG plays a major role in the excitation and heating of the

$\sim 100$  K molecular  $\text{H}_2$  gas, the  $\sim 10^4$  K ionized  $[\text{Ne II}]/[\text{Ne III}]$  gas, the dust grains responsible for the IR continuum, and the smaller PAH grains responsible for the broad PAH features. This is in contrast to other cool cores, which require an additional source of particle heating.

5. The other primary heating mechanism is the AGN at the center of the BCG. This also contributes substantially to the heating of the IR continuum, the ionized gas, as well as the hotter phases (see i.e. R25).
6. Other heating mechanisms, such as cosmic rays, suprathermal ICM particles, and magnetohydrodynamic waves, may also be present, but at suppressed importance relative to the general cool core population.
7. We have uncovered an apparent PAH deficit in the  $\gtrsim 10^{11} M_{\odot}$  cool core BCG population, causing their PAH-based SFRs to be underpredicted by up to an order of magnitude. This is distinct from the deficit found in galaxies with strong AGN like Phoenix, as the other BCGs in the sample all show little to no signs of AGN activity. This may be a result of suprathermal ICM particle heating, creating a harsh environment unsuitable for the sustained existence of PAH grains.

We have not only provided updated measurements and constraints for the SFR and the molecular gas mass, two vital quantities in evaluating the efficiency of cooling, but we have also shown through a correlation analysis that Phoenix more strongly resembles a starburst galaxy than it does any of the other cool core BCGs. This provides even more evidence to suggest that the Phoenix cluster is experiencing a highly efficient, but still turbulent and chaotic, top-down cascade of condensation and cooling from the hot ICM down to the cold molecular phase. We are seeing the effects of this cooling propagate through the young stellar population and into the interstellar radiation field, imprinting signatures onto the molecular gas and PAH emission.

1 This work is based on observations with the  
 2 NASA/ESA/CSA James Webb Space Telescope ob-  
 3 tained from the Data Archive at the Space Telescope  
 4 Science Institute, which is operated by the Associa-  
 5 tion of Universities for Research in Astronomy, Incor-  
 6 porated, under NASA contract NAS 5-03127. Support  
 7 for Program number JWST-GO-02439.001-A was pro-  
 8 vided through a grant from the STScI under NASA con-  
 9 tract NAS 5-03127. M Reeve acknowledges support from  
 10 the National Science Foundation Graduate Research Fel-  
 11 lowship under Grant No. 2141064. M Chatzikos ac-  
 12 knowledges support from NASA (19-ATP19-0188, 22-  
 13 ADAP22-0139) and NSF (1910687). MG acknowl-  
 14 edges support from the ERC Consolidator Grant *Black-*  
 15 *HoleWeather* (101086804). HRR acknowledges an Anne  
 16 McLaren Fellowship from the University of Notting-  
 17 ham.

*Facilities: JWST*

*Software:* `julia` (Bezanson et al. 2017), `LOKI.jl` (<https://github.com/Michael-Reeve/Loki.jl>), `python` (Van Rossum & Drake 2009), `numpy` (Harris et al. 2020), `scipy` (Virtanen et al. 2020), `astropy` (Astropy Collaboration et al. 2013), `matplotlib` (Hunter 2007), `SAOImage DS9` (Smithsonian Astrophysical Observatory 2000)

REFERENCES

- Allamandola, L. J., Tielens, A. G. G. M., & Barker, J. R. 1985, *ApJL*, 290, L25, doi: [10.1086/184435](https://doi.org/10.1086/184435)
- Allen, S. W. 1995, *MNRAS*, 276, 947, doi: [10.1093/mnras/276.3.947](https://doi.org/10.1093/mnras/276.3.947)
- Astropy Collaboration, Robitaille, T. P., Tollerud, E. J., et al. 2013, *A&A*, 558, A33, doi: [10.1051/0004-6361/201322068](https://doi.org/10.1051/0004-6361/201322068)
- Bezanson, J., Edelman, A., Karpinski, S., & Shah, V. B. 2017, *SIAM Review*, 59, 65, doi: [10.1137/141000671](https://doi.org/10.1137/141000671)
- Bolatto, A. D., Wolfire, M., & Leroy, A. K. 2013, *ARA&A*, 51, 207, doi: [10.1146/annurev-astro-082812-140944](https://doi.org/10.1146/annurev-astro-082812-140944)
- Boquien, M., Burgarella, D., Roehlly, Y., et al. 2019, *A&A*, 622, A103, doi: [10.1051/0004-6361/201834156](https://doi.org/10.1051/0004-6361/201834156)
- Boulanger, F., Boissel, P., Cesarsky, D., & Ryter, C. 1998, *A&A*, 339, 194
- Brandl, B. R., Bernard-Salas, J., Spoon, H. W. W., et al. 2006, *ApJ*, 653, 1129, doi: [10.1086/508849](https://doi.org/10.1086/508849)
- Calura, F., Pipino, A., & Matteucci, F. 2008, *A&A*, 479, 669, doi: [10.1051/0004-6361:20078090](https://doi.org/10.1051/0004-6361:20078090)
- Calzadilla, M. S., Bleem, L. E., McDonald, M., et al. 2023, *ApJ*, 947, 44, doi: [10.3847/1538-4357/acc6c2](https://doi.org/10.3847/1538-4357/acc6c2)
- Calzetti, D., Wu, S. Y., Hong, S., et al. 2010, *ApJ*, 714, 1256, doi: [10.1088/0004-637X/714/2/1256](https://doi.org/10.1088/0004-637X/714/2/1256)
- Canizares, C. R., Markert, T. H., & Donahue, M. E. 1988, in *NATO Advanced Study Institute (ASI) Series C, Vol. 229, Cooling Flows in Clusters and Galaxies*, ed. A. C. Fabian, 63, doi: [10.1007/978-94-009-2953-1\\_7](https://doi.org/10.1007/978-94-009-2953-1_7)
- Crawford, C. S., Allen, S. W., Ebeling, H., Edge, A. C., & Fabian, A. C. 1999, *MNRAS*, 306, 857, doi: [10.1046/j.1365-8711.1999.02583.x](https://doi.org/10.1046/j.1365-8711.1999.02583.x)
- Dale, D. A., Gil de Paz, A., Gordon, K. D., et al. 2007, *ApJ*, 655, 863, doi: [10.1086/510362](https://doi.org/10.1086/510362)
- David, L. P., Nulsen, P. E. J., McNamara, B. R., et al. 2001, *ApJ*, 557, 546, doi: [10.1086/322250](https://doi.org/10.1086/322250)
- Donahue, M., de Messières, G. E., O’Connell, R. W., et al. 2011, *ApJ*, 732, 40, doi: [10.1088/0004-637X/732/1/40](https://doi.org/10.1088/0004-637X/732/1/40)
- Donahue, M., Connor, T., Fogarty, K., et al. 2015, *ApJ*, 805, 177, doi: [10.1088/0004-637X/805/2/177](https://doi.org/10.1088/0004-637X/805/2/177)
- Downes, D., & Solomon, P. M. 1998, *ApJ*, 507, 615, doi: [10.1086/306339](https://doi.org/10.1086/306339)
- Downes, D., Solomon, P. M., & Radford, S. J. E. 1993, *ApJL*, 414, L13, doi: [10.1086/186984](https://doi.org/10.1086/186984)

- Draine, B. T., & Li, A. 2007, *ApJ*, 657, 810, doi: [10.1086/511055](https://doi.org/10.1086/511055)
- Edge, A. C. 2001, *MNRAS*, 328, 762, doi: [10.1046/j.1365-8711.2001.04802.x](https://doi.org/10.1046/j.1365-8711.2001.04802.x)
- Edwards, L. O. V., Hudson, M. J., Balogh, M. L., & Smith, R. J. 2007, *MNRAS*, 379, 100, doi: [10.1111/j.1365-2966.2007.11910.x](https://doi.org/10.1111/j.1365-2966.2007.11910.x)
- Fabian, A. C. 2012, *ARA&A*, 50, 455, doi: [10.1146/annurev-astro-081811-125521](https://doi.org/10.1146/annurev-astro-081811-125521)
- Fabian, A. C., Ferland, G. J., Sanders, J. S., et al. 2022, *MNRAS*, 515, 3336, doi: [10.1093/mnras/stac2003](https://doi.org/10.1093/mnras/stac2003)
- Fabian, A. C., Nulsen, P. E. J., & Canizares, C. R. 1984, *Nature*, 310, 733, doi: [10.1038/310733a0](https://doi.org/10.1038/310733a0)
- Fabian, A. C., Sanders, J. S., Ferland, G. J., et al. 2023, *MNRAS*, 521, 1794, doi: [10.1093/mnras/stad507](https://doi.org/10.1093/mnras/stad507)
- Farrah, D., Bernard-Salas, J., Spoon, H. W. W., et al. 2007, *ApJ*, 667, 149, doi: [10.1086/520834](https://doi.org/10.1086/520834)
- Förster Schreiber, N. M., Roussel, H., Sauvage, M., & Charmandaris, V. 2004, *A&A*, 419, 501, doi: [10.1051/0004-6361:20040963](https://doi.org/10.1051/0004-6361:20040963)
- Gaspari, M., Melioli, C., Brighenti, F., & D’Ercole, A. 2011, *MNRAS*, 411, 349, doi: [10.1111/j.1365-2966.2010.17688.x](https://doi.org/10.1111/j.1365-2966.2010.17688.x)
- Gaspari, M., Tombesi, F., & Cappi, M. 2020, *Nature Astronomy*, 4, 10, doi: [10.1038/s41550-019-0970-1](https://doi.org/10.1038/s41550-019-0970-1)
- Gaspari, M., McDonald, M., Hamer, S. L., et al. 2018, *ApJ*, 854, 167, doi: [10.3847/1538-4357/aaaa1b](https://doi.org/10.3847/1538-4357/aaaa1b)
- Harris, C. R., Millman, K. J., van der Walt, S. J., et al. 2020, *Nature*, 585, 357, doi: [10.1038/s41586-020-2649-2](https://doi.org/10.1038/s41586-020-2649-2)
- Hatch, N. A., Crawford, C. S., & Fabian, A. C. 2007, *MNRAS*, 380, 33, doi: [10.1111/j.1365-2966.2007.12009.x](https://doi.org/10.1111/j.1365-2966.2007.12009.x)
- Hicks, A. K., & Mushotzky, R. 2005, *ApJL*, 635, L9, doi: [10.1086/499123](https://doi.org/10.1086/499123)
- Hlavacek-Larrondo, J., McDonald, M., Benson, B. A., et al. 2015, *ApJ*, 805, 35, doi: [10.1088/0004-637X/805/1/35](https://doi.org/10.1088/0004-637X/805/1/35)
- Ho, L. C., & Keto, E. 2007, *ApJ*, 658, 314, doi: [10.1086/511260](https://doi.org/10.1086/511260)
- Hoffer, A. S., Donahue, M., Hicks, A., & Barthelmy, R. S. 2012, *ApJS*, 199, 23, doi: [10.1088/0067-0049/199/1/23](https://doi.org/10.1088/0067-0049/199/1/23)
- Hunter, J. D. 2007, *Computing in Science & Engineering*, 9, 90, doi: [10.1109/MCSE.2007.55](https://doi.org/10.1109/MCSE.2007.55)
- Kaneda, H., Onaka, T., Sakon, I., et al. 2008, *ApJ*, 684, 270, doi: [10.1086/590243](https://doi.org/10.1086/590243)
- Kaviraj, S., Ting, Y.-S., Bureau, M., et al. 2012, *MNRAS*, 423, 49, doi: [10.1111/j.1365-2966.2012.20957.x](https://doi.org/10.1111/j.1365-2966.2012.20957.x)
- Kennicutt, Robert C., J. 1990, in *Astrophysics and Space Science Library*, Vol. 161, *The Interstellar Medium in Galaxies*, ed. J. Thronson, Harley A. & J. M. Shull, 405–435, doi: [10.1007/978-94-009-0595-5\\_17](https://doi.org/10.1007/978-94-009-0595-5_17)
- Kennicutt, Robert C., J. 1998, *ARA&A*, 36, 189, doi: [10.1146/annurev.astro.36.1.189](https://doi.org/10.1146/annurev.astro.36.1.189)
- Klein, M., Mohr, J. J., & Davies, C. T. 2024, *A&A*, 690, A322, doi: [10.1051/0004-6361/202451203](https://doi.org/10.1051/0004-6361/202451203)
- Leger, A., & Puget, J. L. 1984, *A&A*, 137, L5
- Li, Y., Ruszkowski, M., & Bryan, G. L. 2017, *ApJ*, 847, 106, doi: [10.3847/1538-4357/aa88c1](https://doi.org/10.3847/1538-4357/aa88c1)
- Madau, P., & Dickinson, M. 2014, *ARA&A*, 52, 415, doi: [10.1146/annurev-astro-081811-125615](https://doi.org/10.1146/annurev-astro-081811-125615)
- McDonald, M., Benson, B., Veilleux, S., Bautz, M. W., & Reichardt, C. L. 2013, *ApJL*, 765, L37, doi: [10.1088/2041-8205/765/2/L37](https://doi.org/10.1088/2041-8205/765/2/L37)
- McDonald, M., Gaspari, M., McNamara, B. R., & Tremblay, G. R. 2018, *ApJ*, 858, 45, doi: [10.3847/1538-4357/aabace](https://doi.org/10.3847/1538-4357/aabace)
- McDonald, M., Veilleux, S., Rupke, D. S. N., & Mushotzky, R. 2010, *ApJ*, 721, 1262, doi: [10.1088/0004-637X/721/2/1262](https://doi.org/10.1088/0004-637X/721/2/1262)
- McDonald, M., Bayliss, M., Benson, B. A., et al. 2012, *Nature*, 488, 349, doi: [10.1038/nature11379](https://doi.org/10.1038/nature11379)
- McDonald, M., Swinbank, M., Edge, A. C., et al. 2014, *ApJ*, 784, 18, doi: [10.1088/0004-637X/784/1/18](https://doi.org/10.1088/0004-637X/784/1/18)
- McDonald, M., McNamara, B. R., van Weeren, R. J., et al. 2015, *ApJ*, 811, 111, doi: [10.1088/0004-637X/811/2/111](https://doi.org/10.1088/0004-637X/811/2/111)
- McDonald, M., McNamara, B. R., Voit, G. M., et al. 2019, *ApJ*, 885, 63, doi: [10.3847/1538-4357/ab464c](https://doi.org/10.3847/1538-4357/ab464c)
- McNamara, B. R., & Nulsen, P. E. J. 2007, *ARA&A*, 45, 117, doi: [10.1146/annurev.astro.45.051806.110625](https://doi.org/10.1146/annurev.astro.45.051806.110625)
- McNamara, B. R., & O’Connell, R. W. 1989, *AJ*, 98, 2018, doi: [10.1086/115275](https://doi.org/10.1086/115275)
- Micelotta, E. R., Jones, A. P., & Tielens, A. G. G. M. 2010, *A&A*, 510, A37, doi: [10.1051/0004-6361/200911683](https://doi.org/10.1051/0004-6361/200911683)
- Mittal, R., Whelan, J. T., & Combes, F. 2015, *MNRAS*, 450, 2564, doi: [10.1093/mnras/stv754](https://doi.org/10.1093/mnras/stv754)
- Mo, H., van den Bosch, F. C., & White, S. 2010, *Galaxy Formation and Evolution*
- Molendi, S., Tozzi, P., Gaspari, M., et al. 2016, *A&A*, 595, A123, doi: [10.1051/0004-6361/201628338](https://doi.org/10.1051/0004-6361/201628338)
- O’Dea, C. P., Baum, S. A., Privon, G., et al. 2008, *ApJ*, 681, 1035, doi: [10.1086/588212](https://doi.org/10.1086/588212)
- Peeters, E., Spoon, H. W. W., & Tielens, A. G. G. M. 2004, *ApJ*, 613, 986, doi: [10.1086/423237](https://doi.org/10.1086/423237)
- Peterson, J. R., Kahn, S. M., Paerels, F. B. S., et al. 2003, *ApJ*, 590, 207, doi: [10.1086/374830](https://doi.org/10.1086/374830)
- Prasad, D., Sharma, P., & Babul, A. 2015, *ApJ*, 811, 108, doi: [10.1088/0004-637X/811/2/108](https://doi.org/10.1088/0004-637X/811/2/108)
- Rawle, T. D., Edge, A. C., Egami, E., et al. 2012, *ApJ*, 747, 29, doi: [10.1088/0004-637X/747/1/29](https://doi.org/10.1088/0004-637X/747/1/29)
- Roche, P. F., Aitken, D. K., Smith, C. H., & Ward, M. J. 1991, *MNRAS*, 248, 606, doi: [10.1093/mnras/248.4.606](https://doi.org/10.1093/mnras/248.4.606)
- Roussel, H., Helou, G., Hollenbach, D. J., et al. 2007, *ApJ*, 669, 959, doi: [10.1086/521667](https://doi.org/10.1086/521667)

- Russell, H. R., McNamara, B. R., Edge, A. C., et al. 2013, MNRAS, 432, 530, doi: [10.1093/mnras/stt490](https://doi.org/10.1093/mnras/stt490)
- Russell, H. R., McDonald, M., McNamara, B. R., et al. 2017, ApJ, 836, 130, doi: [10.3847/1538-4357/836/1/130](https://doi.org/10.3847/1538-4357/836/1/130)
- Sakon, I., Onaka, T., Ishihara, D., et al. 2004, ApJ, 609, 203, doi: [10.1086/420919](https://doi.org/10.1086/420919)
- Salomé, P., & Combes, F. 2003, A&A, 412, 657, doi: [10.1051/0004-6361:20031438](https://doi.org/10.1051/0004-6361:20031438)
- Salomé, P., Revaz, Y., Combes, F., et al. 2008, A&A, 483, 793, doi: [10.1051/0004-6361:200809412](https://doi.org/10.1051/0004-6361:200809412)
- Sloan, G. C., Hayward, T. L., Allamandola, L. J., et al. 1999, ApJL, 513, L65, doi: [10.1086/311906](https://doi.org/10.1086/311906)
- Smith, J. D. T., Draine, B. T., Dale, D. A., et al. 2007, ApJ, 656, 770, doi: [10.1086/510549](https://doi.org/10.1086/510549)
- Smithsonian Astrophysical Observatory. 2000, SAOImage DS9: A utility for displaying astronomical images in the X11 window environment, Astrophysics Source Code Library, record ascl:0003.002
- Spilker, J. S., Phadke, K. A., Aravena, M., et al. 2023, Nature, 618, 708, doi: [10.1038/s41586-023-05998-6](https://doi.org/10.1038/s41586-023-05998-6)
- Sutherland, R. S., & Dopita, M. A. 1993, ApJS, 88, 253, doi: [10.1086/191823](https://doi.org/10.1086/191823)
- Timmerman, R., van Weeren, R. J., McDonald, M., et al. 2021, A&A, 646, A38, doi: [10.1051/0004-6361/202039075](https://doi.org/10.1051/0004-6361/202039075)
- Togi, A., & Smith, J. D. T. 2016, ApJ, 830, 18, doi: [10.3847/0004-637X/830/1/18](https://doi.org/10.3847/0004-637X/830/1/18)
- Treyer, M., Schiminovich, D., Johnson, B. D., et al. 2010, ApJ, 719, 1191, doi: [10.1088/0004-637X/719/2/1191](https://doi.org/10.1088/0004-637X/719/2/1191)
- Van Kerckhoven, C., Hony, S., Peeters, E., et al. 2000, A&A, 357, 1013
- Van Rossum, G., & Drake, F. L. 2009, Python 3 Reference Manual (Scotts Valley, CA: CreateSpace)
- Veilleux, S., Rupke, D. S. N., Kim, D. C., et al. 2009, ApJS, 182, 628, doi: [10.1088/0067-0049/182/2/628](https://doi.org/10.1088/0067-0049/182/2/628)
- Viaene, S., Nersesian, A., Fritz, J., et al. 2020, A&A, 638, A150, doi: [10.1051/0004-6361/202037476](https://doi.org/10.1051/0004-6361/202037476)
- Virtanen, P., Gommers, R., Oliphant, T. E., et al. 2020, Nature Methods, 17, 261, doi: [10.1038/s41592-019-0686-2](https://doi.org/10.1038/s41592-019-0686-2)
- Werle, A., Poggianti, B., Moretti, A., et al. 2022, ApJ, 930, 43, doi: [10.3847/1538-4357/ac5f06](https://doi.org/10.3847/1538-4357/ac5f06)
- Williamson, R., Benson, B. A., High, F. W., et al. 2011, ApJ, 738, 139, doi: [10.1088/0004-637X/738/2/139](https://doi.org/10.1088/0004-637X/738/2/139)
- Wittor, D., & Gaspari, M. 2020, MNRAS, 498, 4983, doi: [10.1093/mnras/staa2747](https://doi.org/10.1093/mnras/staa2747)
- Wu, Y., Helou, G., Armus, L., et al. 2010, ApJ, 723, 895, doi: [10.1088/0004-637X/723/1/895](https://doi.org/10.1088/0004-637X/723/1/895)
- Xie, Y., & Ho, L. C. 2019, ApJ, 884, 136, doi: [10.3847/1538-4357/ab4200](https://doi.org/10.3847/1538-4357/ab4200)
- . 2022, ApJ, 925, 218, doi: [10.3847/1538-4357/ac32e2](https://doi.org/10.3847/1538-4357/ac32e2)
- Yang, G., Boquien, M., Buat, V., et al. 2020, MNRAS, 491, 740, doi: [10.1093/mnras/stz3001](https://doi.org/10.1093/mnras/stz3001)